JOURNAL OF GEOPHYSICAL RESEARCH, VOL. 108, NO. C8, 3270, doi:10.1029/2002JC001306, 2003

Three-dimensional effects in shear waves

Qun Zhao and I. A. Svendsen
Ocean Engineering Laboratory, Center for Applied Coastal Research, University of Delaware, Newark, Delaware, USA

Kevin Haas
Regional Engineering Program, Georgia Institute of Technology, Savannah, Georgia, USA

Received 16 January 2002; revised 21 February 2003; accepted 2 April 2003; published 22 August 2003.

[1] Most studies on shear waves to date have assumed the flow is depth uniform (two dimensional). In the present study, we utilize the quasi-three-dimensional (quasi-3D) nearshore circulation model SHORECIRC to study shear waves. Our results show that shear wave flow is more organized in the quasi-3D simulation than in the 2D simulation. In the 2D simulation, the vortices are moving farther offshore of the bar, while in the quasi-3D simulation, they are more confined to the shoreward side of the bar. Moreover, the shear waves in the quasi-3D simulation are much less energetic than in the 2D simulation, though the total momentum mixing for the two cases is not significantly different. To understand which mechanisms cause the differences in the 2D and the quasi-3D simulation, the momentum, kinetic energy, and enstrophy equations for the mean flow and the shear waves are derived. The momentum, energy, and enstrophy balances are discussed using the numerical results from the idealized SUPERDUCK topography and the wave conditions on October 16, 1986. The effects of the quasi-3D dispersion due to the depth varying currents on shear waves are illustrated. Analysis of the mean momentum balance shows that both the shear waves and the quasi-3D current pattern contribute to the momentum transfer, and the momentum transfer provided by the shear waves is sometimes larger than that by the quasi-3D dispersive terms. The kinetic energy balance of the shear waves shows that the quasi-3D dispersive terms will extract kinetic energy from the depth-averaged shear waves. Furthermore, the enstrophy equation demonstrates that the quasi-3D dispersion terms provide vortex tilting, which allows three-dimensional vortex interactions. *INDEX TERMS:* 4516 Oceanography: Physical: Eastern boundary currents; 4512 Oceanography: Physical: Currents; 4568 Oceanography: Physical: Turbulence, diffusion, and mixing processes; *KEYWORDS:* shear waves, quasi-3D model, SHORECIRC, three-dimensional effects, dispersive mixing, kinetic energy budget

Citation: Zhao, Q., I. A. Svendsen, and K. Haas, Three-dimensional effects in shear waves, *J. Geophys. Res.*, *108*(C8), 3270, doi:10.1029/2002JC001306, 2003.

1. Introduction

[2] Shear waves were first identified by *Oltman-Shay et al.* [1989]. Since then, they have been studied intensively. A state-of-art review is presented by *Dodd et al.* [2000]. Most of these studies are either based on linear stability analysis [*Bowen and Holman*, 1989; *Dodd et al.*, 1992; *Putrevu and Svendsen*, 1992; *Falqués and Iranzo*, 1994, etc.] or based on direct simulation of finite amplitude shear waves by using the nonlinear shallow water equations [*Deigaard et al.*, 1994; *Allen et al.*, 1996; *Slinn et al.*, 1998; *Özkan-Haller and Kirby*, 1999 (hereinafter referred to as ÖK99)]. This essentially means the flow is considered depth uniform (2D).

[3] Lateral mixing is incorporated in some of these models in a classic way by using an eddy viscosity. It is found that, in general, including the ‘‘lateral mixing,’’ whether a constant eddy viscosity coefficient [*Deigaard et al.*, 1994] or a cross-shore varying eddy viscosity (ÖK99), causes a damping of the shear waves.

[4] The ‘‘lateral mixing’’ used in these models is always specified a priori as an empirical coefficient. However, *Svendsen and Putrevu* [1994] discovered that a major part of the lateral mixing in longshore currents is caused by the depth variation of the currents. This so-called dispersive mixing is deterministic and is caused by the three-dimensional current pattern. Therefore the classic approach to mimic mixing is only an empirical remedy. It has also been found that shear waves themselves provide extensive lateral mixing, which has the effect of modifying the original cross-shore distribution of the mean longshore current (ÖK99).

[5] The initiation of shear waves studied analytically by small-amplitude instability theory describes the shear waves as essentially sinusoidal modulations on the initially uniform longshore current that grow exponentially with time [*Bowen and Holman*, 1989; *Dodd and Thornton*,

0148-0227/03/2002JC001306$09.00

1990; *Dodd et al.*, 1992; *Dodd*, 1994, etc.]. However, numerical simulations such as the works quoted above show that as the modulations grow they change character and eventually split up while shedding vortices with vertical vorticity. Under some conditions, free vortices are even found to propagate away from the shear zone where they are generated. Thus, when fully developed as in the numerical simulations, shear waves are strong vortical motions. However, three-dimensional vortex interaction is missing in the two-dimensional depth averaged models. In these models the vortices are depth-uniform circulation patterns. Hence several physical mechanisms are left out in a two-dimensional simulation.

[6] The purpose of this work is to investigate the role of the three-dimensional depth variation of the currents which is representable for the dispersive mixing on the shear wave development. It is worthwhile to emphasize that the currents vary not just in magnitude over the depth but also, more importantly, in directions. To achieve this, 2D and quasi-3D numerical experiments are carried out simultaneously, and with similar representations in the 2D and the quasi-3D simulations for mechanisms such as the wave driver, bottom friction, turbulence modeling, etc.

[7] The paper is arranged as follows. Section 2 gives a brief introduction of the quasi-3D nearshore circulation model SHORECIRC (hereinafter referred to as SC)[*Van Dongeren and Svendsen*, 2000; *Svendsen et al.*, 2002] used in the computations. In section 3 we first show that using the stripped-down 2D version of the model similar to the model used by ÖK99, we obtain time series at a fixed point for the surface elevation $\bar{\zeta}$ and the cross-shore and longshore velocities $\tilde{V}_x$, $\tilde{V}_y$, respectively, that are remarkably similar to the time series published by ÖK99 for the same situation. A similar discussion was given by *Sancho and Svendsen* [1998] and serves to verify the compatibilities of the two models in spite of their radically different numerical solution techniques. Then, in section 4, two-dimensional and three-dimensional numerical experiments of shear waves are carried out simultaneously. To facilitate comparisons with earlier work, we use the same idealized SUPERDUCK topography used by ÖK99. The momentum balance, energy and enstrophy budget for the shear waves are discussed in sections 5, 6, and 7 and applied to characterize the features of the three-dimensional shear wave system. The discussions and summary are presented in section 8. The derivation of the kinetic energy and enstrophy equations noted in separations for the mean flow and the shear waves are presented in Appendices A and B, respectively.

2. Description of the Model

[8] Following *Putrevu and Svendsen* [1999] (hereinafter referred to as PS99), we split the instantaneous horizontal velocity $u_\alpha(x, y, z, t)$ into three components

$$u_\alpha(x,y,z,t) = u'_\alpha(x,y,z,t) + u_{w\alpha}(x,y,z,t) + V_\alpha(x,y,z,t). \quad (1)$$

The x and y denote the cross-shore and longshore coordinates, and $\alpha(\beta) = 1, 2$ represent these horizontal coordinates, while z is the vertical coordinate. In the above, u'_α, $u_{w\alpha}$, V_α are the turbulent component, the wave component, and the current component, respectively. We then further split the current velocity into the depth-uniform part and the depth-varying part,

$$V_\alpha(x,y,z,t) = \tilde{V}_\alpha(x,y,t) + V_{1\alpha}(x,y,z,t). \quad (2)$$

where the tilde denotes the depth-uniform part and is defined as

$$\tilde{V}_\alpha(x,y,t) = \frac{1}{h}\overline{\int_{-h_0}^{\zeta} u_\alpha(x,y,z,t)dz} = \frac{\bar{Q}_\alpha(x,y,t)}{h}, \quad (3)$$

in which the overbar denotes averaging over the short-wave period, h_0 and ζ represent the still water depth and the instantaneous water surface elevation, respectively. Here $h = h_0 + \bar{\zeta}$ is the total water depth, and $\bar{Q}_\alpha$ is the total volume flux.

[9] The second component of the short-wave-averaged velocity $V_{1\alpha}(x, y, z, t)$ accounts for the vertical variation of the current and satisfies

$$\overline{\int_{-h_0}^{\zeta} V_{1\alpha}dz} = -\overline{\int_{\zeta_t}^{\zeta} u_{w\alpha}dz} = -Q_{w\alpha}, \quad (4)$$

where $Q_{w\alpha}$ is the short-wave-induced volume flux, and ζ_t is the surface elevation of the wave trough level. A sketch of this split of current velocity is shown in Figure 1.

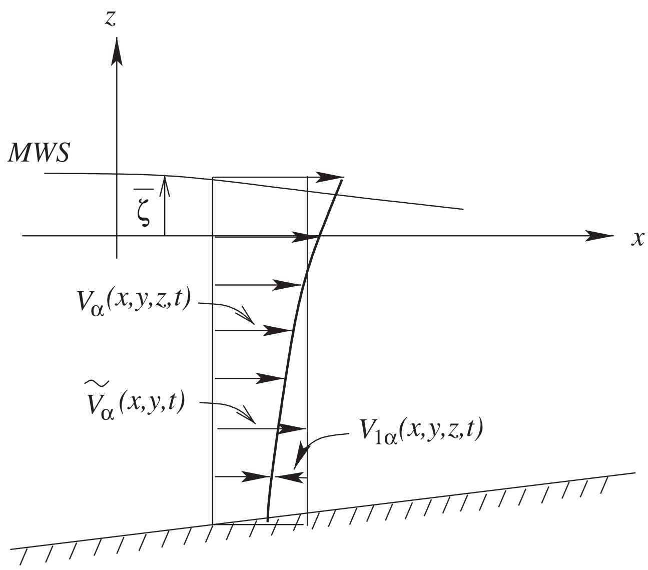

Figure 1. Sketch showing definition of current velocities, where the total current velocity is defined as $V_\alpha(x, y, z, t)$, the depth-uniform part of the current velocity is defined as $\tilde{V}_\alpha(x, y, t)$, and the depth-varying current velocity is $V_{1\alpha}(x, y, z, t)$.

[10] Then the depth-integrated, short-wave-averaged governing equations read (PS99)

$$\frac{\partial\bar{\zeta}}{\partial t} + \frac{\partial}{\partial x_\beta}\left(\tilde{V}_\beta h\right) = 0 \quad (5)$$

$$\frac{\partial}{\partial t}\left(\tilde{V}_\alpha h\right) + \frac{\partial}{\partial x_\beta}\left(\tilde{V}_\alpha\tilde{V}_\beta h\right) + \frac{1}{\rho}\frac{\partial S_{\beta\alpha}}{\partial x_\beta} - \frac{1}{\rho}\frac{\partial T_{\beta\alpha}}{\partial x_\beta} + \frac{1}{\rho}\frac{\partial L_{\beta\alpha}}{\partial x_\beta} + gh\frac{\partial\bar{\zeta}}{\partial x_\alpha} + \frac{\tau^B_\alpha}{\rho} = 0, \quad (6)$$

where $S_{\beta\alpha}$ is the short-wave-induced radiation stress.

[11] Hence solution of equations (5) and (6) will provide information over the horizontal domain of the variation of the mean water surface and the depth-averaged current $\tilde{V}_\alpha$. In the simulations discussed in the following we use REF/DIF1 [*Kirby and Dalrymple*, 1994] as the wave driver to determine radiation stress and short-wave-induced volume flux $Q_{w\alpha}$. These quantities are computed using the linear theory outside the surf zone and augmented by the roller model of *Svendsen* [1984] inside the surf zone [*Svendsen et al.*, 2002].

[12] Solution of equations (5) and (6) requires, however, that we determine $L_{\beta\alpha}$, which is the contribution from the depth-varying currents, the quasi-3D dispersive term.

$$L_{\beta\alpha} = \rho\left[\overline{\int_{-h_0}^{\zeta} V_{1\alpha}V_{1\beta}dz} + \overline{\int_{\zeta_t}^{\zeta}\left(u_{w\alpha}V_{1\beta} + u_{w\beta}V_{1\alpha}\right)dz}\right]. \quad (7)$$

[13] To obtain the vertical profile of depth-varying current, starting from local (non-depth-integrated) horizontal momentum equation, we assume the short-wave-averaged pressure is hydrostatic. This is common in all circulation models and is justified by the fact that the vertical current velocities are found to be small. (This does not mean the vertical velocities W are neglected. As shown by PS99, W is included in all continuity-related considerations (see also equation (10).) The governing equation for the depth-varying current $V_{1\alpha}$ can be written as (PS99)

$$\frac{\partial V_{1\alpha}}{\partial t} - \frac{\partial}{\partial z}\left(\nu_t\frac{\partial V_{1\alpha}}{\partial z}\right) = F_\alpha^{(0)} + F_\alpha^{(1)} + F_\alpha^{(2)}, \quad (8)$$

where

$$F_\alpha^{(0)} = \left\{\frac{1}{\rho h}\frac{\partial S_{\beta\alpha}}{\partial x_\beta} - f_\alpha + \frac{\tau_\alpha^B}{\rho h}\right\}, \quad (9)$$

$$F_\alpha^{(1)} = -\left\{\left(\tilde{V}_\beta\frac{\partial V_{1\alpha}}{\partial x_\beta} + V_{1\beta}\frac{\partial \tilde{V}_\alpha}{\partial x_\beta} + V_{1\beta}\frac{\partial V_{1\alpha}}{\partial x_\beta} + W\frac{\partial V_{1\alpha}}{\partial z}\right) - \frac{1}{\rho h}\frac{\partial L_{\beta\alpha}}{\partial x_\beta}\right\}, \quad (10)$$

$$F_\alpha^{(2)} = \frac{\partial}{\partial x_\beta}\left[\nu_t\left(\frac{\partial V_\alpha}{\partial x_\beta} + \frac{\partial V_\beta}{\partial x_\alpha}\right)\right] + \frac{\partial}{\partial z}\left(\nu_t\frac{\partial W}{\partial x_\alpha}\right) + \frac{1}{\rho h}\frac{\partial T_{\beta\alpha}}{\partial x_\beta}, \quad (11)$$

and PS99 showed that

$$F_\alpha^{(0)} \gg F_\alpha^{(1)} \gg F_\alpha^{(2)}. \quad (12)$$

In the above, f_α is the vertically local contribution to the radiation stress,

$$f_\alpha = \frac{\overline{\partial u_{w\alpha}u_{w\beta}}}{\partial x_\beta} + \frac{\overline{\partial w_w u_{w\alpha}}}{\partial z}. \quad (13)$$

[14] In SC, the top and bottom boundary layers are not numerically resolved, their effects are represented by surface and bottom shear stresses, respectively. In the cases simulated here, we have assumed the wind-induced shear stress is zero. The roller effect due to breaking waves, however, is included in the radiation stress and the short-wave-induced volume flux.

[15] Then, at the bottom, the boundary condition for the depth-varying current requires to match the bottom shear stress and satisfy equation (4),

$$\nu_t\frac{\partial V_{1\alpha}}{\partial z}\Big|_{z=-h_0} = \frac{\tau_\alpha^B}{\rho} \qquad \int_{-h_0}^{\bar{\zeta}} V_{1\alpha}dz = -Q_{w\alpha}. \quad (14)$$

[16] Equation (8) along with the boundary conditions (equation (14)) are solved using the perturbation method. Assuming that the currents vary slowly in time and that the eddy viscosity depth is uniform, the depth-varying currents can be integrated analytically. The detailed derivation is presented by PS99. After some algebra, the leading order solution which is in quadratic form, for example, can be written as

$$V_{1\alpha}^{(0)} = d_{1\alpha}\xi^2 + e_{1\alpha}\xi + (f_{1\alpha} + f_{2\alpha}), \quad (15)$$

where ξ is the vertical coordinate measured from the sea bottom to the mean water level,

$$\xi = z + h_0; \qquad -h_0 \le z \le 0, \quad (16)$$

and the coefficients $d_{1\alpha}$, $e_{1\alpha}$, $f_{1\alpha}$, $f_{2\alpha}$ are calculated from

$$d_{1\alpha} = \frac{F_\alpha^{(0)}}{2\nu_t}, \quad (17)$$

$$e_{1\alpha} = \frac{\tau_\alpha^B}{\rho\nu_t}, \quad (18)$$

$$f_{1\alpha} + f_{2\alpha} = -\left(\frac{d_{1\alpha}}{3}h^2 + e_{1\alpha}\frac{h}{2} + \frac{Q_{w\alpha}}{h}\right). \quad (19)$$

$F_\alpha{}^{(0)}$ and f_α are defined in equations (9) and (13), respectively. The vertical profiles in SC are the approximations solved to the second order to the governing equations.

[17] It is noticed that assuming that the eddy viscosity is depth uniform enabled an analytical solution for the depth-varying current part. This seems to be crude. However, we have carried out a numerical solution of the depth-varying current based on Chebyshev polynomials. The preliminary results of currents on a longshore uniform beach show that the current profiles are not sensitive to the eddy viscosity variation over depth for the tested cases. More detailed tests regarding this issue are underway and will be presented separately.

[18] It is also worthwhile to emphasize that $V_{1\alpha}$ is the solution to the basic equation, thus satisfying both the governing equations (momentum and continuity equation at all levels) and the boundary conditions. The errors in the vertical profiles are purely due to the approximation of the solution.

[19] The depth-integrated turbulent shear stresses $T_{\beta\alpha}$ are expressed by an eddy viscosity model,

$$T_{\beta\alpha} = \rho h\nu_t\left(\frac{\partial\tilde{V}_\alpha}{\partial x_\beta} + \frac{\partial\tilde{V}_\beta}{\partial x_\alpha}\right). \quad (20)$$

The eddy viscosity formulation accounts for both wave-breaking and bottom-generated turbulence. The combined contributions to the eddy viscosity from these sources are calculated as

$$\nu_t = C_1 \kappa \sqrt{\frac{f_w}{2}} |u_0| h + Mh \left(\frac{D}{\rho} \right)^{1/3} + \nu_{t,0}. \tag{21}$$

Here the first term represents the effect in the current above the bottom boundary layer. It is based on the works of *Svendsen and Putrevu* [1994] and *Coffey and Nielsen* [1984]. Here κ is the von Karman constant ($\kappa \simeq 0.4$), f_w is the wave-related bottom friction coefficient, and $|u_0|$ is the short-wave particle velocity amplitude evaluated at the bottom. The second term accounts for the effect of wave breaking. It is a modified *Battjes* [1975] model. D is the short-wave energy dissipation per unit area given by the formulation used in the REF/DIF1. The small constant $\nu_{t,0}$ is an empirical measure of the background eddy viscosity found far offshore, given as 1/10 of the bottom friction outside the surf zone. The bottom-induced turbulence is always present, but the second term is only present inside the surf zone. By comparing the eddy viscosity estimates from thisequation with the experimental results of *Nadaoka and Kondoh* [1982] and the values suggested by *Svendsen et al.* [1987], $C_1 \simeq 0.2$ and $M \simeq 0.1$ are being taken.

[20] In the simulations we will discuss in this paper, the general bottom friction in SC is simplified to the linear approximation for the bottom friction used by ÖK99, which is given by

$$\tau_\alpha^B = \frac{2}{\pi} c_f \frac{|u_0|}{h} \tilde{V}_\alpha. \tag{22}$$

Here the parameter c_f is chosen to be 0.0035 as used by ÖK99 for the simulation of SUPERDUCK topography on October 16, 1986. It is noticed that the bottom friction used here is rather simple. However, our study showed that though different formulation of the bottom friction will affect the development of shear waves, the quasi-3D effects on the shear waves due to the vertical variation of the currents remain the same. As in all earlier studies, we also disregard the wave-current interaction due to the shear wave velocities.

[21] The system of the governing equations is solved in its conservation form using an explicit Predictor-Corrector scheme which is third order in time and fourth order in space [*Svendsen et al.*, 2002].

[22] At the offshore boundary, a no-flux boundary condition is applied. To simplify the computation, at the shoreline a wall is placed at a water depth of a few centimeters. The free slip boundary condition is applied on the wall. At the lateral boundaries, a periodic boundary condition is applied.

3. Definition of Shear Wave Quantities

[23] Before we go into the discussions of the quasi-3D effect in shear waves, we have checked the numerical model performances versus previous models, such as that of ÖK99. It is found that when the SC model is reduced to the form of the equations used by ÖK99, and upon using the same forcing conditions, shear wave development on a 1/20 longshore uniform plane beach shows remarkably similar behaviors. In the SC simulation, the grid size dx = 5 m, dy = 5 m in the cross-shore and longshore directions, respectively, are used. The time step, dt = 0.2 s, is calculated to satisfy the CFL condition, with the Courant number set to 0.3 in this case. The time series for the first 12 hours of the surface elevation, the cross-shore and longshore velocity components $\tilde{V}_x$ and $\tilde{V}_y$, are presented in Figure 2 for both the reduced SC model (2D version of SC) and ÖK99 results (without the "lateral mixing").

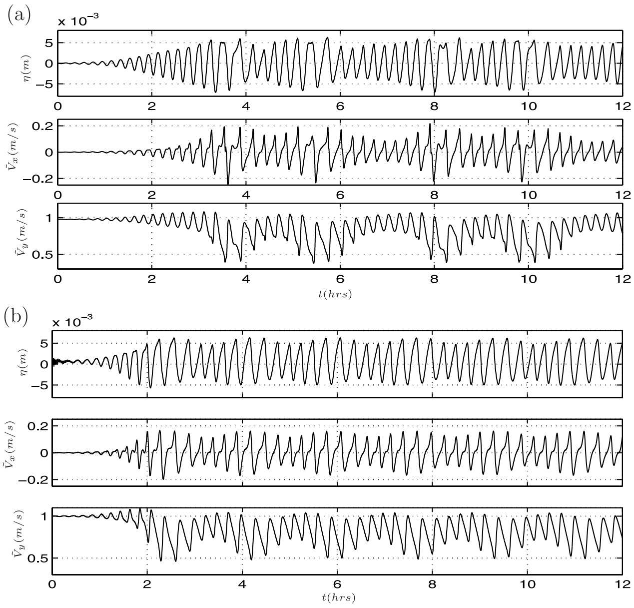

Figure 2. Comparison of 2D models with two different numerical schemes. (a) The 2D version of SHORECIRC. (b) *Özkan-Haller and Kirby* [1999] without the "lateral mixing".

[24] When comparing the two simulations, we see that they show similar features even in many of the smaller details. This essentially is a check of the numerical accuracy of the two models which, while solving the same equations, are based on radically different numerical solution schemes. Similar results were found by *Sancho and Svendsen* [1998].

[25] In the following, we will use the full SC equations to simulate and analyze shear waves on a longshore uniform barred beach. While ÖK99 analyzed the effects of bottom friction and "lateral mixing" on shear waves, we will add the three-dimensionality and analyze its effect on the shear wave development. However, to be able to compare with the ÖK99 results, we will continue to use the same topography as that used by ÖK99, which is from the October 16 SUPERDUCK experiment. Following ÖK99, we form a longshore uniform topography by using measured SUPERDUCK topography from one transect, and assume that this cross-shore profile extends uniformly in the entire longshore region. A three-dimensional sketch of the situation is shown in Figure 3.

[26] In order to further link our computations to the measured results from that of experiment, we also assume that the wave conditions used are similar to the waves measured at the SUPERDUCK experiment, in which the

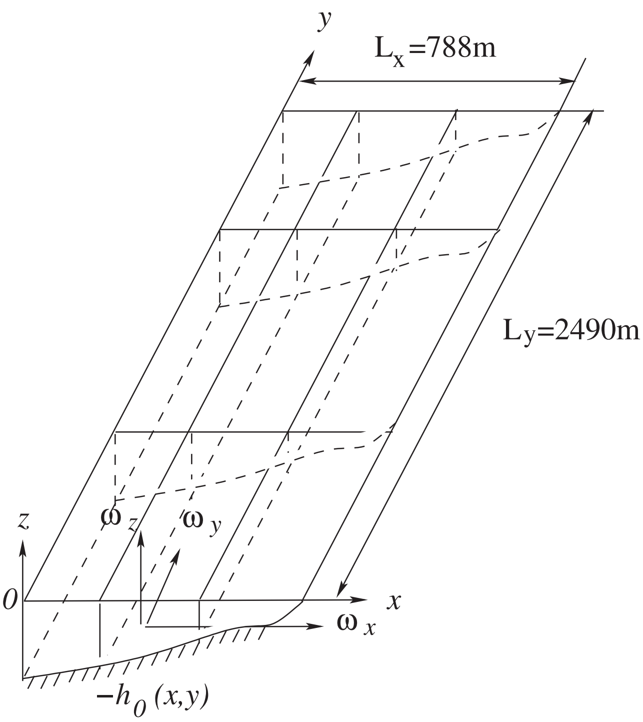

Figure 3. A sketch of idealized topography used in the simulation, and definitions of the coordinates. The cross-shore and longshore domain length are denoted by L_x and L_y, respectively. Here ω_z is the vertical vorticity, and ω_x and ω_y are the two horizontal vorticity components.

root-mean square wave height H_{rms} at 8 m water depth is 0.93 m, with peak frequency f_p = 0.16 HZ and mean incidence angle $\theta = 21°$. The top panel of Figure 4 shows the measured (circle) and simulated (line) wave heights from REF/DIF1. The agreement is satisfactory. The bottom panel in Figure 4 shows the idealized SUPERDUCK topography used in the simulations.

[27] In order to investigate how the quasi-3D dispersive mixing affects the shear waves and how the quasi-3D dispersive mixing and the lateral mixing provided by the shear waves affects each other, 2D and quasi-3D numerical experiments are carried out simultaneously by switching on/off the quasi-3D dispersive terms. All the numerical simulations are performed from a cold start, and in the following, we consider the fully developed motions. They are quasi-steady in the sense that after sufficiently long computation time the average values have become steady.

[28] In order to analyze the numerical simulations of the shear waves, we need to define the shear wave quantities we want to analyze. The definition of the shear wave quantities is not unique; it depends on how we define the "mean" flow quantities. Because the time mean of the motions taken over the timescale of the shear fluctuations continues to evolve slowly even after many hours, the "mean" of a quantity **G** is defined as the instantaneous average over the longshore length L_y of the computational domain. This is meaningful because we use a periodic condition at the cross-shore boundaries, which means we are considering flows that are, in average, longshore uniform. Thus we are able to split the instantaneous quantity **G** into a "mean" flow quantity $\overline{\mathbf{G}}^{L_y}$ and a fluctuation part $\mathbf{G}'$; that is, we write

$$\mathbf{G} = \overline{\mathbf{G}}^{L_y} + \mathbf{G}' \tag{23}$$

$$\overline{\mathbf{G}}^{L_y} = \frac{1}{L_y}\int_0^{L_y} \mathbf{G}dy, \tag{24}$$

where the longshore averaging is denoted by $\overline{\cdot}^{L_y}$. We have the following relations:

$$\frac{1}{L_y}\int_0^{L_y} \mathbf{G}'dy = 0. \tag{25}$$

Notice that the longshore averages for the nonlinear terms are not equal to zero; that is, they do not follow equation (25).

[29] Using the longshore-averaged current as the mean current allows us to investigate the time evolution of shear waves and their effect on the mean current profile over the cross-shore distance. However, because the fully developed shear fluctuations are more random than periodic and L_y is limited, the longshore averaged quantities will still show a weak temporal variation, even at a stage where the overall flow is essentially steady. An example is shown in Figures 5 and 6. For certain results, this variation is eliminated by averaging over a time longer than the shear wave timescale, and this is marked by $\langle \overline{\cdot}^{L_y} \rangle$.

4. Three-Dimensional Features of Shear Waves

[30] We first look at the instantaneous distribution of flow characteristics in the numerical simulation for the same flow conditions using 2D and quasi-3D versions of the SC model system. Figure 7 shows instantaneous distributions ("snap shots") of the vorticity contours and the kinetic energy contours at two time intervals; in particular, we consider the depth-averaged vertical vorticity $\tilde{\omega}'_z$ and the kinetic energy $\tilde{k}'$ of the shear waves, respectively, which are defined as

$$\tilde{\omega}'_z = \frac{\partial \tilde{V}'_y}{\partial x} - \frac{\partial \tilde{V}'_x}{\partial y} \tag{26}$$

$$\tilde{k}' = \frac{\tilde{V}'^2_x + \tilde{V}'^2_y}{2}. \tag{27}$$

[31] The top panels are the depth-averaged (marked by tilde) shear wave vertical vorticity contours $\tilde{\omega}'_z$, while the bottom panels are the depth-averaged shear wave kinetic energy contours $\tilde{k}'$. The four left-hand panels are results from the quasi-3D simulation, and the results from the 2D simulation are presented at the right.

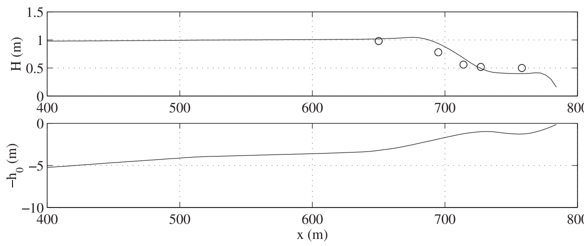

Figure 4. (top) Cross-shore distribution of wave height: circles, data; line, result from REF/DIF 1. (bottom) Idealized SUPERDUCK topography.

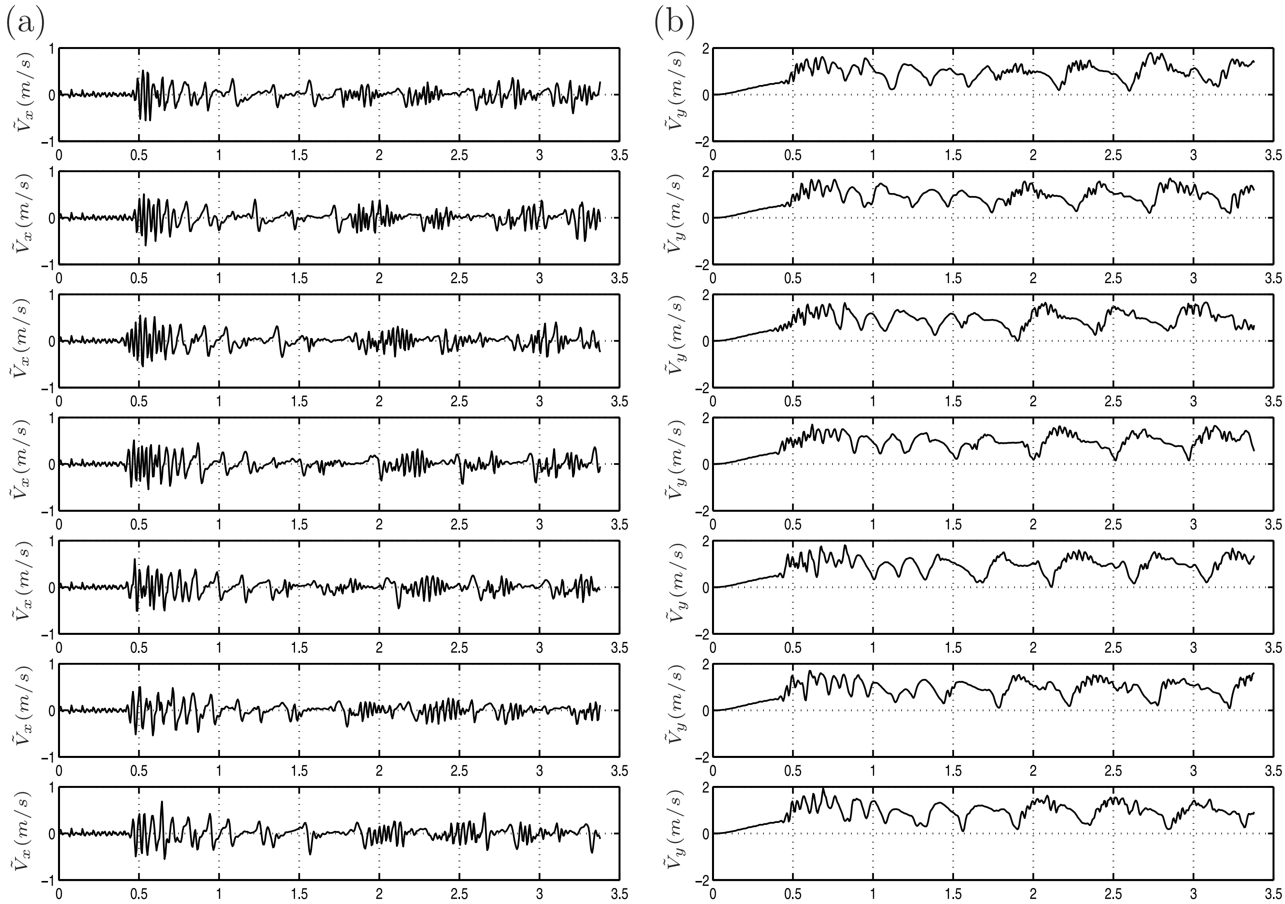

Figure 5. Time series of instantaneous current velocities at cross-shore location x = 749 m. (a) Depth-averaged cross-shore velocities. (b) Depth-averaged long-shore velocities. From top to bottom: current velocities at longshore location $y = \frac{1}{8}L_y, \frac{2}{8}L_y, \frac{3}{8}L_y, \frac{4}{8}L_y, \frac{5}{8}L_y, \frac{6}{8}L_y, \frac{7}{8}L_y$.

[32] Though there are clearly similarities between the 2D and the quasi-3D simulations, the vertical vorticity fields in Figure 7 show that the shear wave flow is more organized in the quasi-3D simulation than in the 2D simulation. In the 2D simulation, the vortices are moving farther offshore of the bar, while in the quasi-3D simulation they are confined closer to the bar where they were originally generated. Furthermore, the strength of the vorticity in the quasi-3D simulation is weaker than that in the 2D simulation. This is measured by integrating the enstrophy, half square of the vorticity $\frac{\tilde{\omega}_z'\tilde{\omega}_z'}{2}$, over

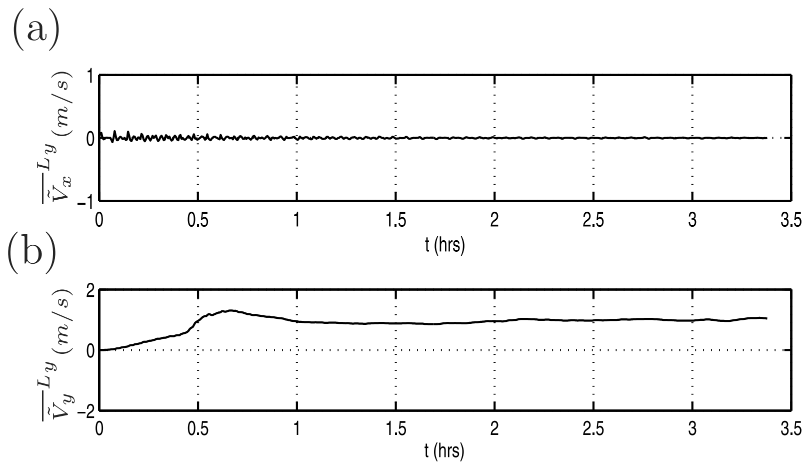

Figure 6. Instantaneous longshore-averaged current at cross-shore location x = 749 m. (a) Depth-averaged cross-shore velocities. (b) Depth-averaged long-shore velocities.

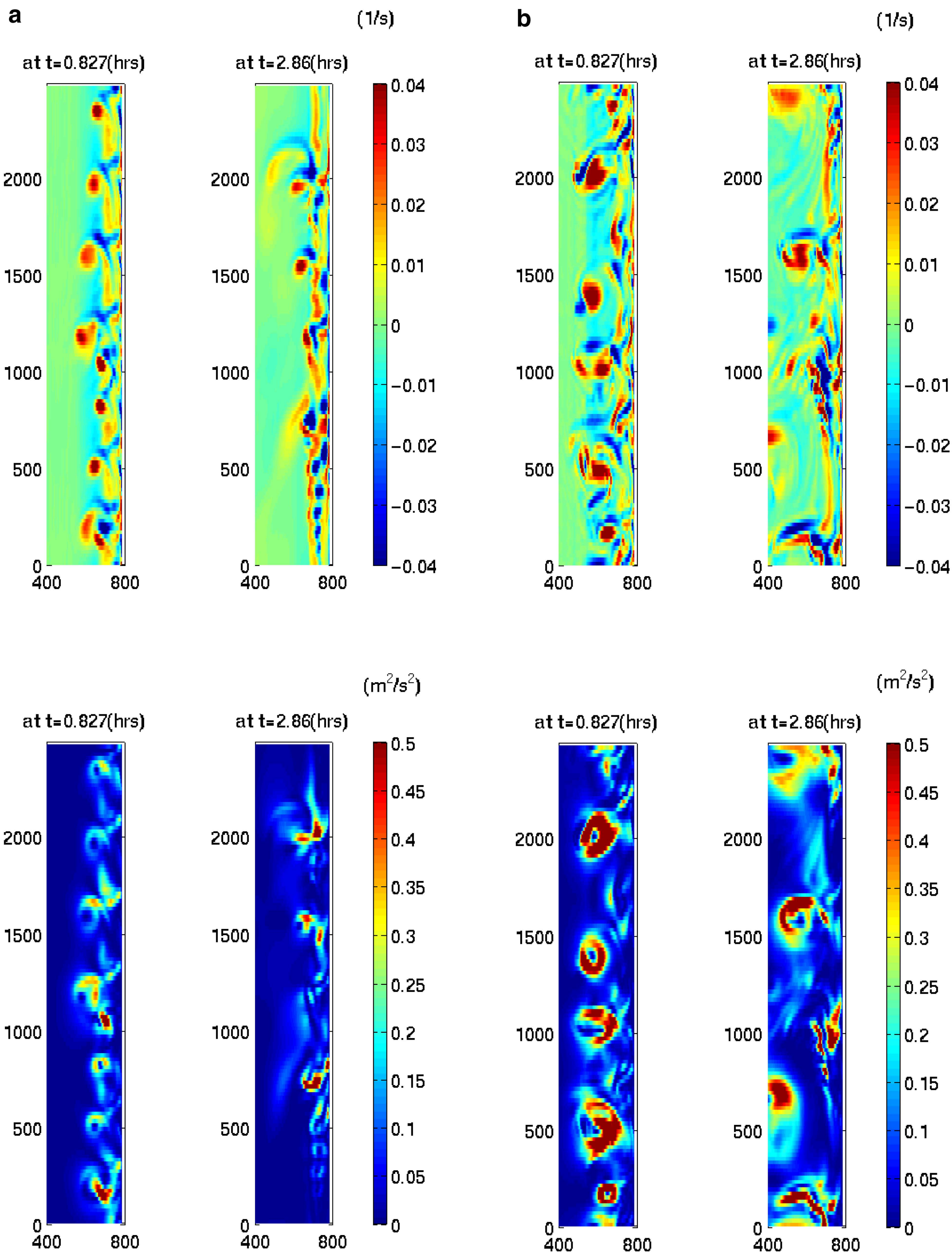

Figure 7. (top) Instantaneous distribution of depth-averaged (marked by tilde) shear wave vertical vorticity $\tilde{\omega}'_z = \frac{\partial \tilde{V}'_y}{\partial x} - \frac{\partial \tilde{V}'_x}{\partial y}$ and (bottom) kinetic energy $\tilde{k}' = \frac{\tilde{V}'^2_x + \tilde{V}'^2_y}{2}$ of (left-hand panels of each part) the quasi-3D simulation and (right-hand panels of each part) the 2D simulation. The beach is to the right and the flow is moving upward.

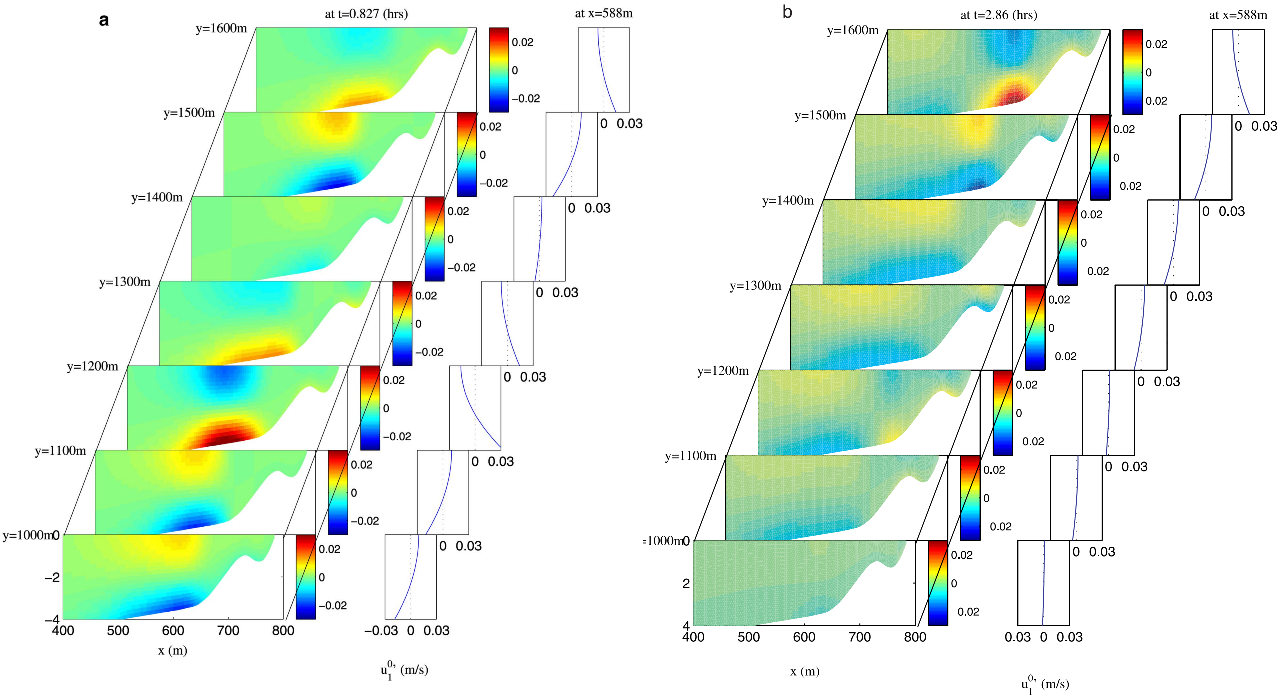

Figure 8. Instantaneous contours of the depth-varying cross-shore shear wave velocity $V_{x1}^{(0)\prime}$ along cross-shore section with different longshore positions from the quasi-3D simulation. The times are the same as in Figure 7.

the whole computational domain. The results for the two times of the snapshots are 0.9559 ($1/s^2$) and 1.0262 ($1/s^2$) for the quasi-3D simulation, and 1.6249 ($1/s^2$) and 1.6083 ($1/s^2$), respectively, for the 2D simulation. Similarly, kinetic energies integrated over the whole domain at the times of the snapshots, are 652.8 (m^4/s^2) and 561.6 (m^4/s^2), respectively, for the quasi-3D simulation, and 1478.4 (m^4/s^2) and 2197.7 (m^4/s^2), respectively, for the 2D simulation. Thus the shear waves in the quasi-3D simulation are also less energetic than in the 2D simulation.

[33] Figures 8 and 9 show instantaneous contours of the depth-varying cross-shore and longshore shear wave velocities between $y = 1000$ m and $y = 1600$ m at the same times $t = 0.827$ hours and $t = 2.86$ hours as in Figure 7. In these figures, the contour plots represent the cross-shore section of shear wave velocities at different longshore positions. The details of the depth variation of the current at a specific cross-shore or longshore location are shown to the right of each panel.

[34] Figures 8 and 9 show that at any instant both the cross-shore and the longshore velocities of shear waves exhibit clear depth and longshore dependency. A particularly strong depth variation of the current is observed far offshore of the bar at around $x = 600$ m. Besides, as the color codes indicate, the longshore currents are found at some times to change their signs in the cross-shore direction.

[35] The three-dimensionality of the vorticity is also evident from Figures 10 and 11, which show the snapshots of horizontal shear wave vorticity ω'_x and ω'_y, respectively. The two horizontal vorticity components are defined as

$$\omega'_x = \frac{\partial W'}{\partial y} - \frac{\partial V'_y}{\partial z} \qquad \omega'_y = \frac{\partial V'_x}{\partial z} - \frac{\partial W'}{\partial x}. \tag{28}$$

In the above, W' is the vertical velocity of the shear waves fluctuations. The directions of ω'_x and ω'_y are defined in Figure 3. The vertical velocities of the currents are not provided directly by the present model which focus on the horizontal motion, but they can be obtained by the integration of the continuity equation. For the shear wave velocity W' this gives

$$W' = -\int_{-h_0}^{\bar{\zeta}} \left(\frac{\partial V'_x}{\partial x} + \frac{\partial V'_y}{\partial y} \right) dz. \tag{29}$$

The W' values are found to be very small and their contribution to equation (28) is negligible.

[36] Figure 10 presents the horizontal vorticity ω'_x along longshore sections at different cross-shore positions, while Figure 11 pictures the horizontal vorticity ω'_y along cross-shore sections at different alongshore positions. Figures 10 and 11 demonstrate that both ω'_x and ω'_y are depth varying with a linear distribution with zero at the mean water level. This is because only the leading order of the depth-varying current $V_{1\alpha}^{(0)}$, which is of quadratic form as indicated by equation (15), is utilized to analyze the result though the vertical profiles of the current were solved to the second order to the governing equations.

[37] The longshore dependency of ω'_x in Figure 10 is very clear. The ω'_y in Figure 11 also varies in the longshore direction and the locations with stronger vorticity shift in the cross-shore direction with time.

[38] In summary, Figure 7 shows that the difference between the vertical vorticity and the depth-averaged kinetic energy of the shear waves in the 2D and quasi-3D simulation is significant. This is likely due to the three-dimensionality in the quasi-3D simulation as shown in

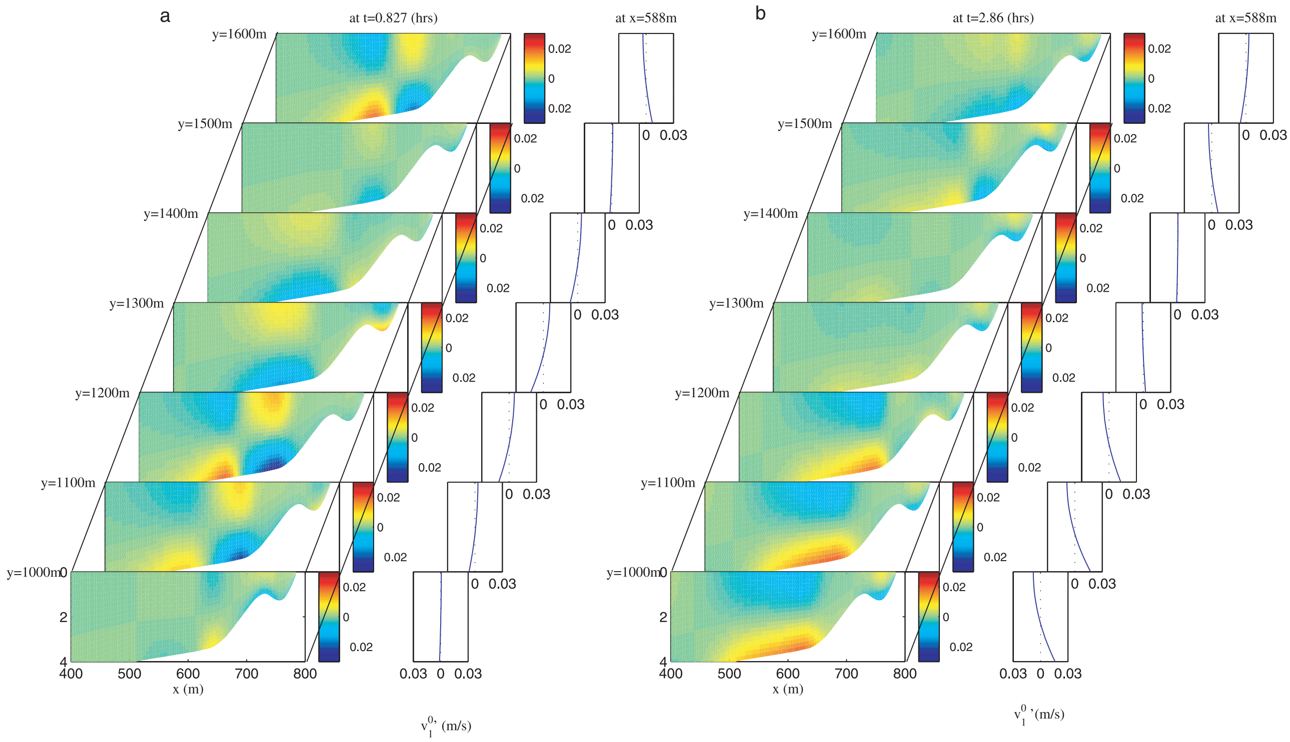

Figure 9. Instantaneous contours of the depth-varying longshore shear wave velocity $V_{y1}^{(0)\prime}$ along cross-shore section with different longshore positions from the quasi-3D simulation. The times are the same as in Figure 7.

Figures 8–11. In the following, we will further analyze the mechanisms behind this.

5. Lateral Mixing and Momentum Balance

[39] One reason that shear waves have attracted so much attention is that they are believed to be a plausible mechanism that could contribute to the horizontal momentum transfer in the nearshore circulation modeling. As mentioned, *Svendsen and Putrevu* [1994] found that the quasi-3D structure of currents will also introduce momentum transfer by a mechanism which is similar to the dispersion effect discovered by *Taylor* [1954], and which can be one order larger than the momentum transfer provided by the

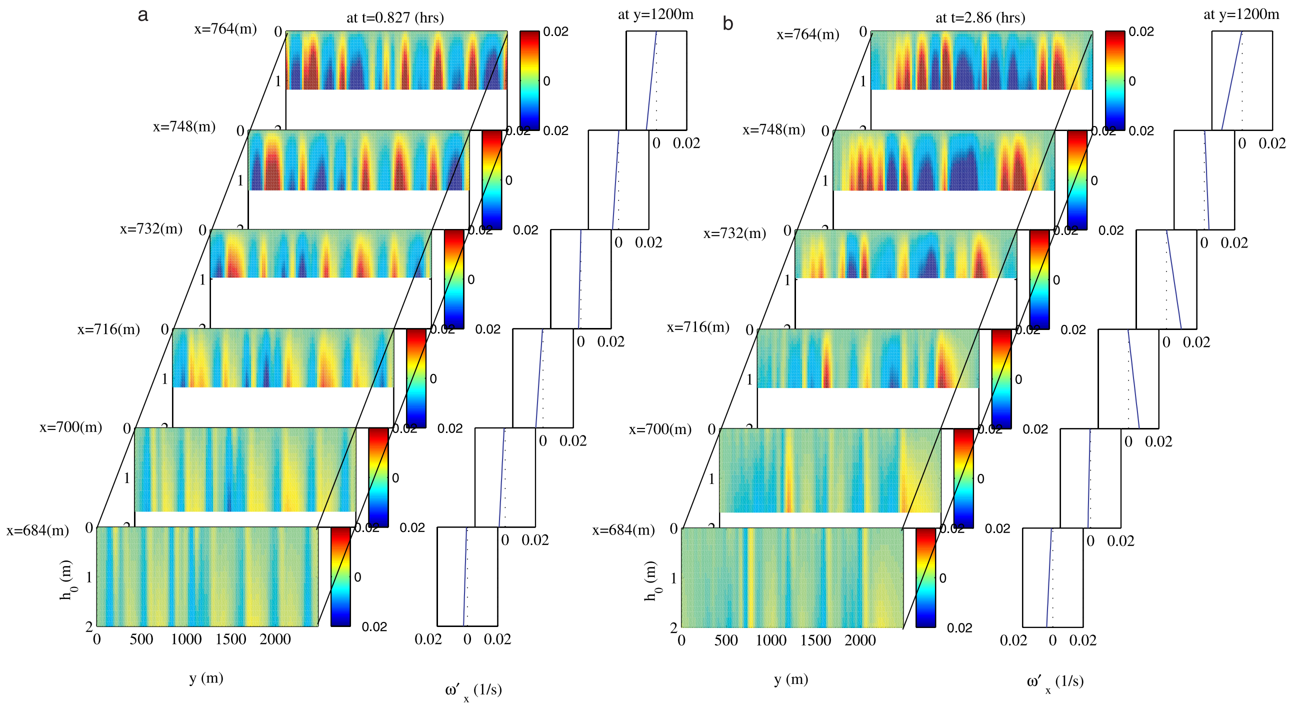

Figure 10. Instantaneous snapshots of shear wave horizontal vorticity $\omega'_x = \frac{\partial W'}{\partial y} - \frac{\partial V'_y}{\partial z}$ along longshore sections with different cross-shore positions. The times are the same as in Figure 7.

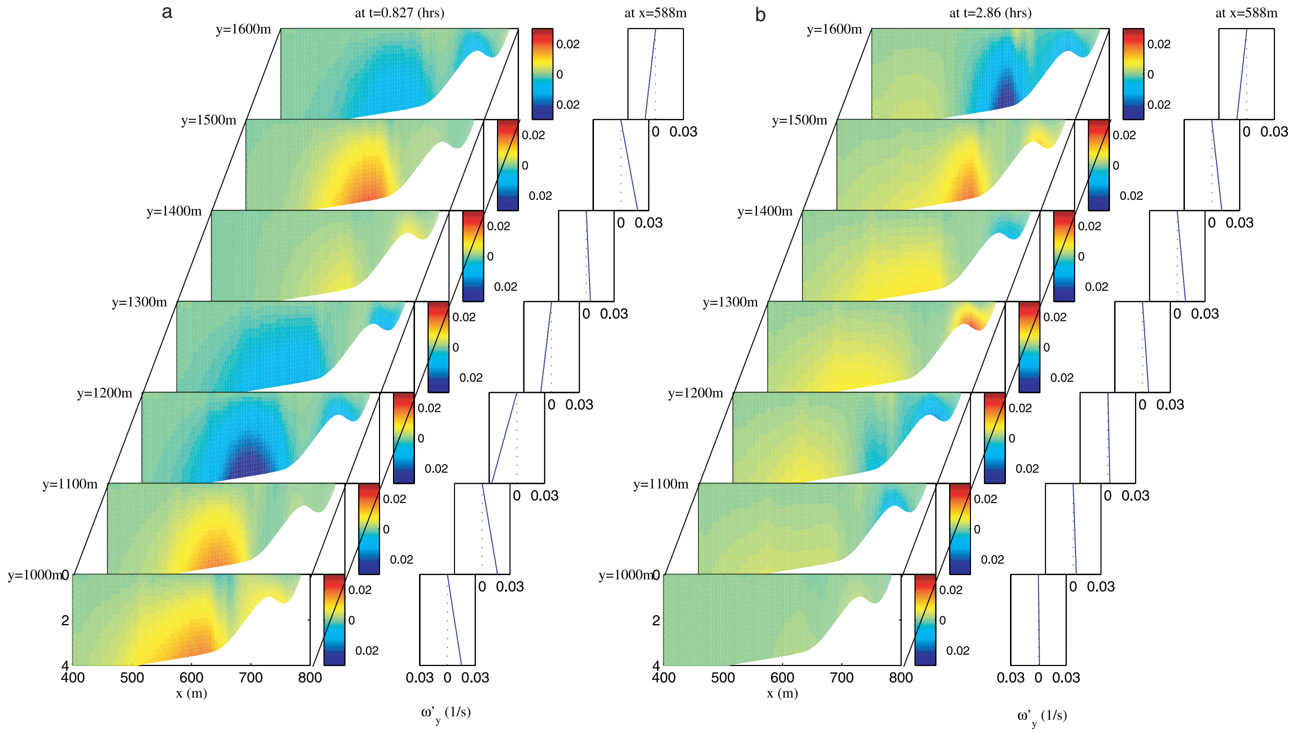

Figure 11. Instantaneous snapshots of shear wave horizontal vorticity $\omega'_y = \frac{\partial V'_x}{\partial z} - \frac{\partial W'}{\partial x}$ along cross-shore sections with different longshore positions. The times are the same as in Figure 7.

turbulence. In this section, we will investigate the magnitude of the momentum transfer provided by the depth-varying current through the quasi-3D dispersive terms and the shear waves, and how these mechanisms interact with each other. To define the problem, we need to derive the mean and the shear wave momentum equations.

[40] Using equation (23) to split the velocities into the longshore-averaged and the fluctuating parts in the continuity and momentum equations (5) and (6), and performing longshore averaging ($\overline{\cdot}^{L_y}$) using equation (24) gives the depth-integrated continuity and momentum equations for the longshore-averaged flow,

$$\frac{\partial}{\partial t}\overline{\overline{\zeta}}^{L_y} + \frac{\partial}{\partial x_\beta}\left(\overline{\tilde{V}_\beta}^{L_y}\overline{h}^{L_y}\right) = 0 \tag{30}$$

$$\begin{aligned}\frac{\partial}{\partial t}\left(\overline{\tilde{V}_\alpha}^{L_y}\overline{h}^{L_y}\right) &+ \frac{\partial}{\partial x}\left(\overline{\tilde{V}_\alpha}^{L_y}\overline{\tilde{V}_x}^{L_y}\overline{h}^{L_y}\right)\\ &= \frac{1}{\rho}\frac{\partial}{\partial x}\left(-\overline{S_{x\alpha}}^{L_y} + \overline{T_{x\alpha}}^{L_y} - \overline{L_{x\alpha}}^{L_y}\right)\\ &\quad - \frac{\overline{\tau^B_\alpha}^{L_y}}{\rho} - g\overline{h}^{L_y}\frac{\partial\overline{\overline{\zeta}}^{L_y}}{\partial x_\alpha} - \frac{\partial}{\partial x}\left(\overline{\tilde{V}'_\alpha\tilde{V}'_x}^{L_y}\overline{h}^{L_y}\right),\end{aligned} \tag{31}$$

where β is a dummy index and the subscript $_x$ denotes the component in the cross-shore (x) direction. Here we have neglected the surface elevation for the shear waves, i.e., $h' = 0$, to simplify the derivation. Also, since we have turned off the wave-current interaction due to shear wave velocities, the terms related to the perturbation of radiation stress is zero.

[41] The term $-\frac{\partial}{\partial x}(\overline{\tilde{V}'_\alpha\tilde{V}'_x}^{L_y}\overline{h}^{L_y})$ in the mean momentum equation (31) provides momentum transfer from the shear waves to the mean flow. It is similar to the role of Reynolds stresses in the Reynolds-averaged equations. The term $-\frac{1}{\rho}\frac{\partial\overline{L_{x\alpha}}^{L_y}}{\partial x}$ represents quasi-3D current-current contribution to the momentum transfer due to the depth-varying current ("dispersive mixing").

[42] In the following, we will investigate how the quasi-3D dispersive term and the shear waves affect one another. To achieve this, we will first average equation (31) over timescales sufficiently longer than the shear wave timescale (marked by $\langle\cdot\rangle$),

$$\begin{aligned}\left\langle\frac{\partial}{\partial x}\left(\overline{\tilde{V}_\alpha}^{L_y}\overline{\tilde{V}_x}^{L_y}\overline{h}^{L_y}\right)\right\rangle &= -\left\langle\frac{1}{\rho}\frac{\partial}{\partial x}\overline{S_{x\alpha}}^{L_y}\right\rangle + \left\langle\frac{1}{\rho}\frac{\partial}{\partial x}\overline{T_{x\alpha}}^{L_y}\right\rangle\\ &\quad - \left\langle\frac{1}{\rho}\frac{\partial}{\partial x}\overline{L_{x\alpha}}^{L_y}\right\rangle - \left\langle\frac{\overline{\tau^B_\alpha}^{L_y}}{\rho}\right\rangle\\ &\quad - \left\langle g\overline{h}^{L_y}\frac{\partial\overline{\overline{\zeta}}^{L_y}}{\partial x_\alpha}\right\rangle - \left\langle\frac{\partial}{\partial x}\left(\overline{\tilde{V}'_\alpha\tilde{V}'_x}^{L_y}\overline{h}^{L_y}\right)\right\rangle.\end{aligned} \tag{32}$$

[43] We then analyze how the momentum is transferred by the quasi-3D dispersive term ($\langle-\frac{1}{\rho}\frac{\partial\overline{L_{x\alpha}}^{L_y}}{\partial x}\rangle$), and the shear waves ($\langle-\frac{\partial}{\partial x}(\overline{\tilde{V}'_\alpha\tilde{V}'_x}^{L_y}\overline{h}^{L_y})\rangle$), by comparing the magnitude of these two terms. Figure 12 shows the cross-shore distribution of longshore and time-averaged horizontal momentum transfer by the quasi-3D dispersive term ($\langle-\frac{1}{\rho}\frac{\partial\overline{L_{x\alpha}}^{L_y}}{\partial x}\rangle$ (solid lines)) and the shear waves ($\langle-\frac{\partial}{\partial x}\overline{\tilde{V}'_\alpha\tilde{V}'_x}^{L_y}\overline{h}^{L_y}\rangle$ (dashed lines)) in the cross-shore (top panel) and longshore (bottom panel) momentum equations from the quasi-3D simulation. For the case studied here, it shows that in the longshore momentum balance, the momentum transfer provided by the shear waves dominates over the momentum transfer by the quasi-3D dispersive terms. This momentum transfer contributes to the cross-shore variation of the mean longshore current. The quasi-3D dispersive terms, however, provide slightly larger momen-

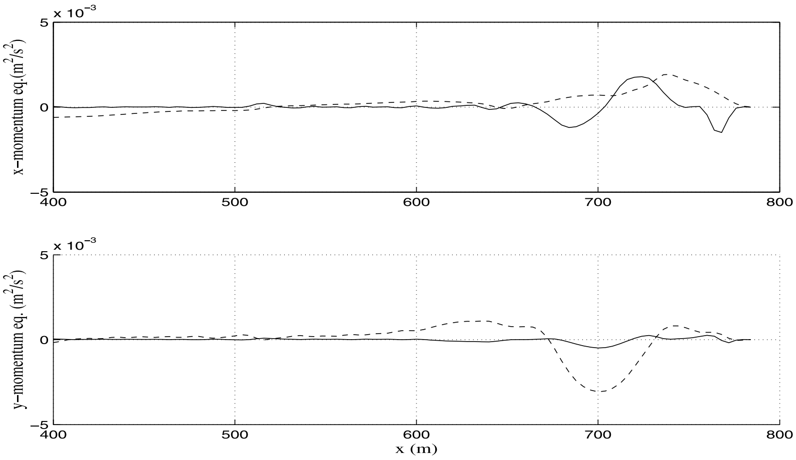

Figure 12. Cross-shore distribution of time and longshore-averaged horizontal momentum transfer by the quasi-3D dispersive term $(\langle -\frac{1}{\rho}\frac{\partial \overline{L_{x\alpha}}^{L_y}}{\partial x}\rangle$ (solid lines)) and by shear waves $(\langle -\frac{\partial}{\partial x}\overline{\tilde{V}'_\alpha \tilde{V}'_x}^{L_y}\overline{h}^{L_y}\rangle$ (dashed lines)) in the (top) cross-shore and (bottom) longshore momentum equations from the quasi-3D simulation, in units of m^2/s^2. The shoreline is at x = 788 m.

tum transfer than that by the shear waves in the cross-shore momentum equation.

[44] We then compare the level of the momentum transfer due to shear waves $(\langle -\frac{\partial}{\partial x}(\overline{\tilde{V}'_\alpha \tilde{V}'_x}^{L_y}\overline{h}^{L_y})\rangle)$ in the 2D and the quasi-3D simulation. The results are shown in Figure 13, where the dashed lines represent the results from the 2D simulation, and the solid lines are the results from the quasi-3D simulation. It shows that the momentum transfer provided by the shear waves in the 2D simulation is larger, and has wider cross-shore extension than that in the quasi-3D simulation. This is consistent with the observation in Figure 7 in that in the 2D case the shear wave energy is spread farther seaward. It is also seen that the difference in the level of momentum transfer between the 2D and quasi-3D simulation is more evident in the cross-shore momentum equation than that in the longshore momentum equation. The computations indicate that this difference is due to the phase shift between $\tilde{V}'_x$ and $\tilde{V}'_y$ in the mixing term $\langle -\frac{\partial}{\partial x}(\overline{\tilde{V}'_\alpha \tilde{V}'_x}^{L_y}\overline{h}^{L_y})\rangle$ in the longshore momentum equation.

[45] The total amount of the momentum transfer in the 2D and quasi-3D simulation are compared in Figure 14. In the 2D case (dashed lines), the total momentum transfer is mainly provided by the shear waves $\langle -\frac{\partial}{\partial x}(\overline{\tilde{V}'_\alpha \tilde{V}'_x}^{L_y}\overline{h}^{L_y})\rangle$, as the turbulence mixing is generally small compared to the shear wave mixing. In the quasi-3D flow situation (solid lines), the momentum transfer is provided by a combination of the shear waves and the quasi-3D dispersion due to the depth varying current. Therefore the total momentum transfer in the quasi-3D simulation is $\langle -\frac{\partial}{\partial x}(\overline{\tilde{V}'_\alpha \tilde{V}'_x}^{L_y}\overline{h}^{L_y})\rangle + \left\langle -\frac{1}{\rho}\frac{\partial \overline{L_{x\alpha}}^{L_y}}{\partial x}\right\rangle$. The figures show large differences in the level of the total cross-shore momentum transfer, in particular, offshore of the bar where the mixing in the quasi-3D case is almost negligible. In the longshore momentum equation, however, only small differences occur. As a consequence, the mean longshore current profiles (Figure 15) for the 2D and quasi-3D simulations also exhibit very small differences. Thus in popular terms one can say it seems that in the case of a 2D simulation the shear wave

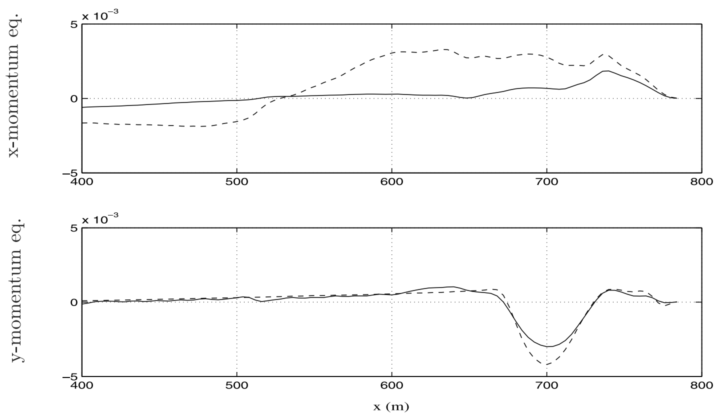

Figure 13. (top) Time averaged cross-shore and (bottom) longshore momentum transfer by the shear waves $(\langle -\frac{\partial}{\partial x}\overline{V'_\alpha V'_x}^{L_y}\overline{h}^{L_y}\rangle)$ from the 2D (dashed lines) and the quasi-3D (solid lines) simulation, in units of m^2/s^2. The shoreline is at x = 788 m.

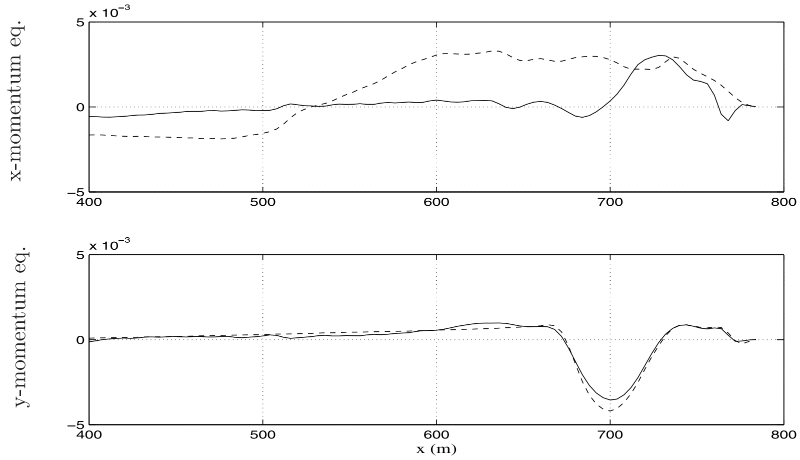

Figure 14. (top) Total momentum transfer in the cross-shore and (bottom) longshore direction from the quasi-3D ($\langle -\frac{\partial}{\partial x}\overline{\tilde{V}'_\alpha \tilde{V}'_x}^{L_y}\overline{h}^{L_y}\rangle + \left\langle -\frac{1}{\rho}\frac{\partial \overline{L_{x\alpha}}^{L_y}}{\partial x}\right\rangle$ (solid lines)) and the 2D ($\langle -\frac{\partial}{\partial x}\overline{\tilde{V}'_\alpha \tilde{V}'_x}^{L_y}\overline{h}^{L_y}\rangle$ (dashed lines)) simulations, in units of m^2/s^2.

intensity increases to compensate for the lack of 3D mixing.

6. Kinetic Energy Budget

[46] The bottom panels of Figure 7 clearly demonstrated that there is a big difference in the kinetic shear wave energy in the 2D and quasi-3D simulation. This leads us to analyze how the shear wave energy is generated in the flow.

[47] The equation for shear wave kinetic energy reads (equation (A9); for derivation, see Appendix A)

$$\int_0^{L_x} \frac{\partial}{\partial t}\left(\frac{\overline{\tilde{V}'_\alpha \tilde{V}'_\alpha}^{L_y}}{2}\overline{h}^{L_y}\right)dx = -\int_0^{L_x} \overline{\tilde{V}'_\alpha \tilde{V}'_x}^{L_y}\overline{h}^{L_y}\frac{\partial \overline{\tilde{V}_\alpha}^{L_y}}{\partial x}dx + \int_0^{L_x}\overline{\frac{\tilde{V}'_\alpha}{\rho}\frac{\partial T'_{\beta\alpha}}{\partial x_\beta}}^{L_y}dx - \int_0^{L_x}\overline{\frac{\tilde{V}'_\alpha}{\rho}\frac{\partial L'_{\beta\alpha}}{\partial x_\beta}}^{L_y}dx - \int_0^{L_x}\overline{\tilde{V}'_\alpha\frac{\tau'^B_\alpha}{\rho}}^{L_y}dx. \tag{33}$$

Here the term on the LHS of equation (33) represents the change of shear wave kinetic energy. On the RHS, the first term represents the production of shear wave kinetic energy by the mean flow (PROD in equation (33)); the next three terms on the RHS represent the work done by turbulent shear stress (TURB), by the quasi-3D dispersive mixing terms (DISP), and by the bottom friction(FRICT), respectively, all due to shear wave velocities. In the case of a 2D simulation, the third term at the RHS would obviously missing.

[48] Equation (33) is the instant kinetic energy equation for the shear waves, and it governs how the shear waves grow with time. In order to investigate how the shear wave energy develops and to illustrate the contribution of each mechanism, particularly the quasi-3D dispersive mixing terms to the shear waves, we computed each term in equation (33) from the numerical simulation.

[49] Figure 16 shows, from top to bottom, the temporal evolution of the shear wave kinetic energy within the computational domain, the shear wave kinetic energy production by the mean flow, and work done by the turbulence, by the quasi-3D dispersion terms and by the bottom friction terms due to shear wave velocities, respectively, corresponding to the four terms on the RHS of equation (33).

[50] The temporal evolution of the shear wave energy shows that there is a surge in the production term at the initial stage in the shear wave development process. After that, the shear wave kinetic energy fluctuates about the mean with a net increase that approaches zero as a steady state develops. The contribution of the production term is always positive, as would be expected. Similarly, the work done by the turbulence and the bottom friction terms are always negative, indicating that they remove energy from the shear waves. Of particular interest, however, is that the

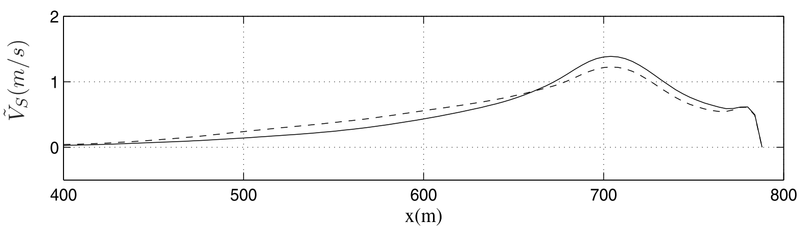

Figure 15. Time-averaged mean longshore current in the 2D (dashed line) and quasi-3D (solid line) simulation.

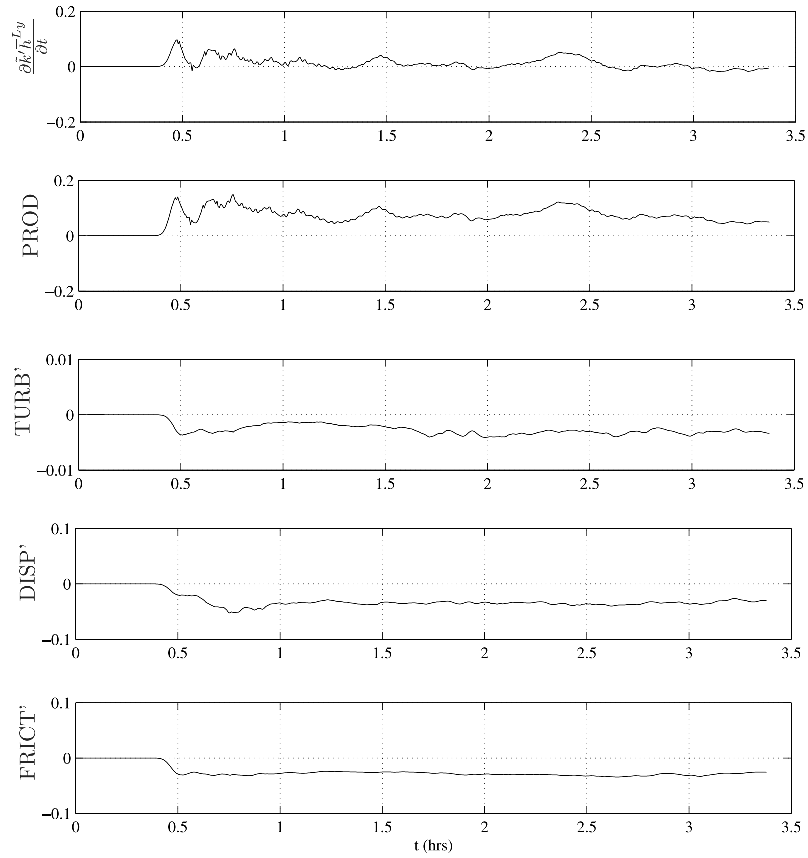

Figure 16. Time evolution of shear wave energy. PROD, production of shear wave kinetic energy by the mean flow; TURB', work done by the turbulence on shear waves; DISP', work done by the quasi-3D dispersive terms on shear waves; FRICT', work done by the bottom friction on shear waves. Units are m^4/s^3.

work done by the quasi-3D dispersive mixing terms associated with the shear waves (the third term in the RHS of equation (33)) is also negative at all times. This indicates that the quasi-3D dispersive mixing terms extract kinetic energy from the depth-averaged shear waves. And as the form of the term implies that this part of the energy is not dissipated to heat but is transferred to the depth-varying current. Furthermore, it is seen that the contribution of the quasi-3D dispersive terms is at least one order larger than the work done by the turbulent shear stress on shear waves but of the same order of magnitude as the contribution from the bottom friction.

[51] An alternative way to illustrate the role of the quasi-3D dispersive mixing terms on the shear waves is to look at the cross-shore distribution of the work done by the quasi-3D dispersive mixing terms, $\langle -\overline{\frac{\tilde{V}'_\alpha}{\rho}\frac{\partial'_{\beta\alpha}}{\partial x_\beta}}^{L_y} \rangle$, on shear waves as shown in the top panel of Figure 17. The $\langle \cdot \rangle$ above indicates long-term averaging over the period after the initial surge. Again, it is seen that the global contribution of the work done by the quasi-3D dispersive terms is negative.

[52] The next question we would ask is does the quasi-3D dispersive mixing terms extract energy from the depth uniform current at every location? To answer this question, we will look at the work done against the longshore-averaged current $\overline{V_\alpha}^{L_y}$ by the longshore-averaged quasi-3D dispersive mixing terms, $\langle -\frac{\overline{V_\alpha}^{L_y}}{\rho}\frac{\partial \overline{L_{x\alpha}}^{L_y}}{\partial x} \rangle$. The bottom panel of Figure 17 shows the time-averaged cross-shore distribution of the work done by the quasi-3D dispersive terms on the longshore-averaged currents $\langle -\frac{\overline{V_\alpha}^{L_y}}{\rho}\frac{\partial \overline{L_{x\alpha}}^{L_y}}{\partial x} \rangle$, which means it represents the exchange of energy between the depth-uniform and the depth-varying part of the longshore-averaged flow. Since Figure 17 shows that this term is overwhelmingly negative over the cross-shore transect, it appears that the $\langle -\frac{\overline{V_\alpha}^{L_y}}{\rho}\frac{\partial \overline{L_{x\alpha}}^{L_y}}{\partial x} \rangle$ term actually transfers kinetic energy from the depth-uniform current to the depth-varying current component.

7. Three-Dimensional Effect in Vertical Vorticity

[53] The top panels in Figure 7 demonstrate differences in the strength of shear wave vertical vorticity in the 2D and the quasi-3D calculations. This is not a surprise, as the vortex dynamics in the 2D and the quasi-3D flow situations is fundamentally different. Vortex tilting, which is a three-dimensional phenomenon, is absent in a 2D simulation. In order to analyze the three-dimensional vorticity balance, the vorticity transport equation needs to be derived. The interactions between the longshore-averaged and the fluctuating vortices, however, can be discussed only in terms of enstrophy, which is defined as the half square of the vorticity, $\frac{\omega_i \omega_i}{2}$.

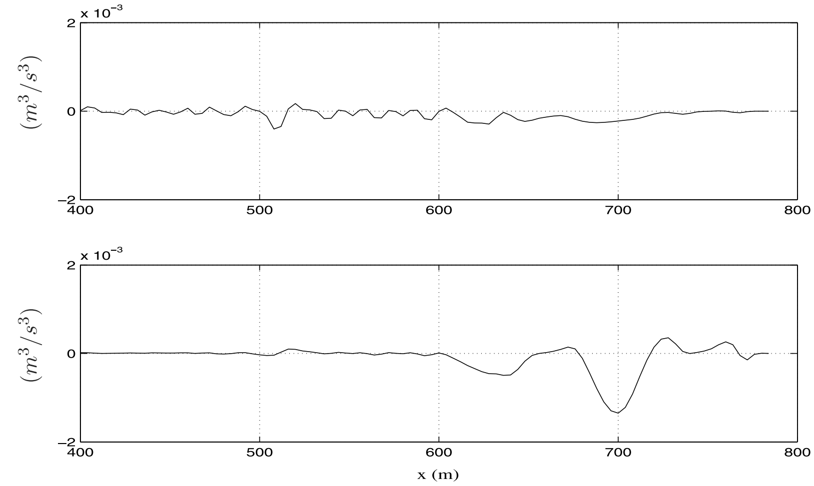

Figure 17. (top) $\langle \overline{-\frac{V'_\alpha}{\rho}\frac{\partial L'_{\beta\alpha}}{\partial x_\beta}}^{L_y} \rangle$: cross-shore distribution of time-averaged work done by the quasi-3D lateral mixing terms on the shear waves. (bottom) $\langle -\frac{\overline{V_\alpha}^{L_y}}{\rho}\frac{\partial \overline{L_{x\alpha}}^{L_y}}{\partial x} \rangle$: cross-shore distribution of time-averaged work done by the quasi-3D lateral mixing terms on the mean currents.

[54] The momentum equation (6) is written in the form

$$\frac{\partial \tilde{V}_\alpha}{\partial t} + \tilde{V}_\beta \frac{\partial \tilde{V}_\alpha}{\partial x_\beta} = -g\frac{\partial \bar{\zeta}}{\partial x_\alpha} - \frac{1}{\rho h}\frac{\partial}{\partial x_\beta}\left(S_{\beta\alpha} - T_{\beta\alpha} + L_{\beta\alpha}\right) - \frac{1}{\rho h}\tau^B_\alpha, \tag{34}$$

where

$$\frac{\partial}{\partial x_\beta}\tilde{V}_\alpha \tilde{V}_\beta h = \tilde{V}_\beta h \frac{\partial \tilde{V}_\alpha}{\partial x_\beta} - \tilde{V}_\alpha \frac{\partial \bar{\zeta}}{\partial t}, \tag{35}$$

in which

$$\frac{\partial h}{\partial t} = \frac{\partial \bar{\zeta}}{\partial t}, \tag{36}$$

and the continuity equation (5) is used.

[55] Taking the curl of equation (34), we get the depth-averaged vertical vorticity transport equation,

$$\frac{\partial \tilde{\omega}_z}{\partial t} + \tilde{V}_\beta \frac{\partial \tilde{\omega}_z}{\partial x_\beta} + \tilde{\omega}_z \frac{\partial \tilde{V}_\beta}{\partial x_\beta} = -\varepsilon_{\beta\alpha z}\frac{\partial}{\partial x_\beta}\frac{1}{\rho h}\frac{\partial}{\partial x_\gamma}\left(S_{\gamma\alpha} - T_{\gamma\alpha} + L_{\gamma\alpha}\right) - \varepsilon_{\beta\alpha z}\frac{\partial}{\partial x_\beta}\frac{\tau^B_\alpha}{\rho h}, \tag{37}$$

where $\tilde{\omega}_z$ is the depth-averaged vertical vorticity, $\varepsilon_{\beta\alpha z}$ is called the alternating tensor or the permutation symbol.

[56] Equation (34) solves the depth-integrated current velocity $\tilde{V}_\alpha$, the effect of depth varying current $V_{1\alpha}$ is hidden in the quasi-3D dispersive terms, $L_{\beta\alpha}$. As a consequence, equation (37) is different from the vorticity transport equation derived from the shallow water equation in that the three-dimensional vortex stretching and tilting is enabled through the quasi-3D dispersive terms. This can be seen clearly when we write equation (37) in the potential vorticity form by using the continuity equation (5).

$$\frac{D}{Dt}\left(\frac{\tilde{\omega}_z}{h}\right) = \frac{1}{h}\left[-\varepsilon_{\beta\alpha z}\frac{\partial}{\partial x_\beta}\frac{1}{\rho h}\frac{\partial}{\partial x_\gamma}\left(S_{\gamma\alpha} - T_{\gamma\alpha} + L_{\gamma\alpha}\right) - \varepsilon_{\beta\alpha z}\frac{\partial}{\partial x_\beta}\frac{\tau^B_\alpha}{\rho h}\right]. \tag{38}$$

[57] Equation (38) demonstrates that the radiation stress term is the source term and the turbulence shear stress and the bottom friction term are the sink terms in the potential vorticity equation. The role of the quasi-3D dispersive term is to provide vortex tilting, which will be shown later this section.

[58] Similar to the shear wave kinetic energy, the depth-integrated enstrophy equation for the shear waves is (equation (B10) in Appendix B),

$$\begin{aligned}\int_0^{L_x}\frac{\partial}{\partial t}\frac{\overline{\tilde{\omega}'_z\tilde{\omega}'_z}^{L_y}\bar{h}^{L_y}}{2}dx = &-\int_0^{L_x}\overline{\tilde{\omega}'_z\tilde{V}'_x}^{L_y}\bar{h}^{L_y}\frac{\partial\overline{\tilde{\omega}_z}^{L_y}}{\partial x}dx\\ &+\int_0^{L_x}\varepsilon_{\beta\alpha z}\bar{h}^{L_y}\overline{\tilde{\omega}'_z\frac{\partial}{\partial x_\beta}\frac{1}{\rho\bar{h}^{L_y}}\frac{\partial T'_{\gamma\alpha}}{\partial x_\gamma}}^{L_y}dx\\ &-\int_0^{L_x}\varepsilon_{\beta\alpha z}\bar{h}^{L_y}\overline{\tilde{\omega}'_z\frac{\partial}{\partial x_\beta}\frac{1}{\rho\bar{h}^{L_y}}\frac{\partial L'_{\gamma\alpha}}{\partial x_\gamma}}^{L_y}dx\\ &-\int_0^{L_x}\varepsilon_{\beta\alpha z}\bar{h}^{L_y}\overline{\tilde{\omega}'_z\frac{\partial}{\partial x_\beta}\frac{\tau'^B_\alpha}{\rho\bar{h}^{L_y}}}^{L_y}dx\\ &-\int_0^{L_x}\bar{h}^{L_y}\overline{\tilde{\omega}'_z\left(\tilde{\omega}'_z\frac{\partial\tilde{V}'_\beta}{\partial x_\beta}+\overline{\tilde{\omega}_z}^{L_y}\frac{\partial\tilde{V}'_\beta}{\partial x_\beta}+\tilde{\omega}'_z\frac{\partial\overline{\tilde{V}_x}^{L_y}}{\partial x}\right)}^{L_y}dx,\end{aligned} \tag{39}$$

where $\tilde{\omega}'_z$ is the depth-averaged vertical vorticity for the shear waves.

[59] In equation (39), the left-hand side represents the change of shear wave vorticity, the first term on the right-hand side is the vorticity production term due to the gradient of the mean vorticity. This term is like the turbulence production term in the energy equation; we call it the gradient production of shear wave vorticity by the mean flow. The next three terms on the right-hand side of the equation are the contribution to the shear wave vorticity due to the turbulent shear stress, the quasi-3D dispersive terms and the bottom friction, respectively. The last line in equation (39) counts for the effect due to the changes of water depth, the two-dimensional vortex stretching/squeezing term, when the continuity equations are used.

[60] The individual terms in equation (39) are shown in Figure 18. The shear wave vorticity is fed by the mean shear through the vorticity production term $-\int_0^{L_x}\overline{\tilde{\omega}'_z\tilde{V}'_x}^{L_y}\bar{h}^{L_y}\frac{\partial\overline{\tilde{\omega}_z}^{L_y}}{\partial x}dx$.

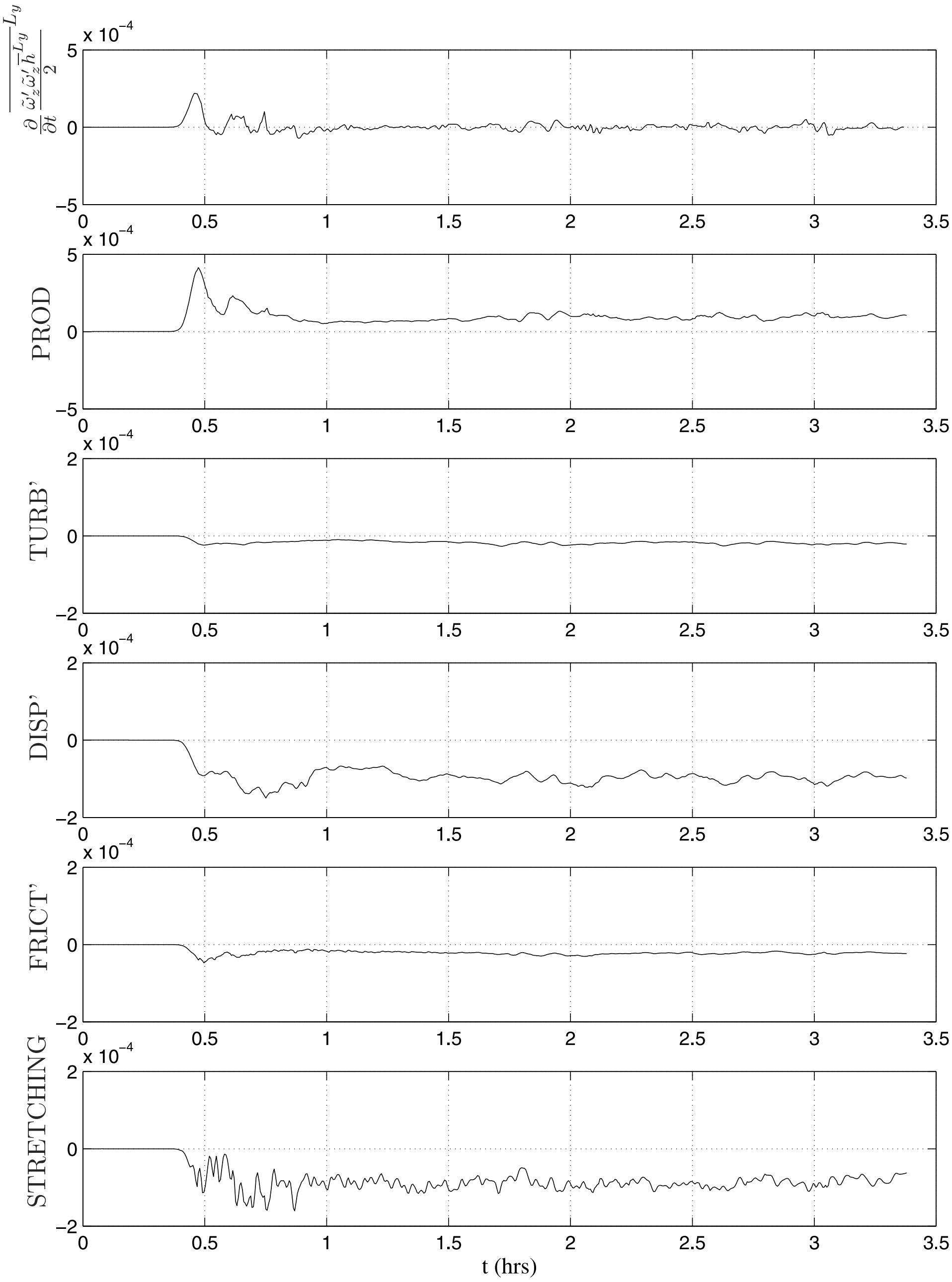

Figure 18. Time evolution of shear wave enstrophy. PROD, production of the shear wave enstrophy by the mean flow; TURB', dissipation of the enstrophy due to the turbulent shear stress. DISP', contribution to the enstrophy due to the 3D dispersive terms; FRICT', dissipation of the enstrophy due to the bottom friction; STRETCHING, contribution to the enstrophy due to the change of water depth. Units are m^2/s^3.

The turbulence and the bottom friction due to the shear waves will dissipate part of the enstrophy. The contribution of the quasi-3D dispersive terms to the shear wave enstrophy equation is always negative. Because the quasi-3D dispersive term is nondissipative as the form implies, this term actually provide vortex tilting. The total vortex stretching/squeezing due to the change of water depth is negative in this case.

8. Summary and Discussions

[61] In this paper, the quasi-3D numerical model SHORECIRC has been utilized to study shear waves. Two-dimensional and quasi-3D numerical experiments are carried out using the idealized SUPERDUCK topography also used by ÖK99. The depth-averaged shear wave quantities in the 2D and quasi-3D simulation showed significant differences when the same conditions are used. In general, the shear waves in the quasi-3D simulation are less energetic than that in the 2D simulation. Moreover, the shear wave vortices are more confined to the nearshore compared to that in the 2D situation. In the quasi-3D simulation the shear wave velocities and the vorticity show clearly three-dimensional characteristics, and three-dimensional vortex tilting is also found in the quasi-3D simulation. These elements are missing in a 2D simulation.

[62] The momentum equations, energy equations, and the enstrophy equations for both the longshore-averaged flow and for the shear wave part are derived to study the different mechanisms in the 2D and quasi-3D simulation, in particular, the effect of the quasi-3D dispersive terms in the shear waves.

[63] The momentum balance shows that both the shear waves and the depth-varying currents provide horizontal momentum transfer to the system. The momentum transfer provided by the shear waves is sometimes stronger than that by the quasi-3D dispersive terms, but generally of the same order of magnitude for the longshore balance in the quasi-3D flow situation. In the cross-shore momentum balance, however, the quasi-3D dispersive terms dominate. In the 2D situation, the momentum transfer provided by the shear waves is much stronger than in the quasi-3D simulation, a finding which is in accordance with the result that the shear wave energy is also much larger in the 2D simulations. However, the total momentum transfer (“lateral mixing”) is approximately the same in the 2D and the quasi-3D simulations in the longshore momentum equation, because in the quasi-3D case the smaller momentum transfer due to smaller shear wave velocity is compensated by the 3D dispersive mixing due to the vertical variation of the currents.

[64] While the shear waves and the quasi-3D dispersion act in parallel in the momentum balance, their functions in the energy balance are quite different. As expected, the analysis of the energy balance for the shear waves shows that the shear wave kinetic energy is first of all extracted from the mean flow through the shear of the longshore current. However, the work done by the quasi-3D dispersive mixing terms on the shear waves extracts kinetic energy from the depth averaged shear waves and transfers it into the depth-varying part of the currents.

[65] The enstrophy balance of the vertical vorticity component of the shear waves shows that the shear wave vorticity is mainly fed by the gradient of the mean vorticity. The contribution of the quasi-3D dispersive terms to the depth-averaged vertical vorticity component is negative. This indicates that the quasi-3D dispersive terms in the vorticity transport equation derived from SC actually provide the three-dimensional vortex tilting.

[66] It is worthwhile to mention that though the present paper presents shear waves in a particular situation using certain bathymetry and frictional coefficient, the results and the conclusions are not limited to this case. To verify this point, we have run shear waves on a longshore uniform plane beach and used different bottom friction coefficients. We found that the conclusions we obtained in this paper generally hold for all tested conditions.

Appendix A: Derivation of the Shear Wave Kinetic Energy Equation

[67] The depth-integrated kinetic energy equation for the longshore-averaged flow is obtained by taking the dot product of equation (31) and $\overline{\tilde{V}_\alpha}^{L_y}$. In the process, we notice that

$$\overline{\tilde{V}_\alpha}^{L_y}\frac{\partial}{\partial t}\left(\overline{\tilde{V}_\alpha}^{L_y}\overline{h}^{L_y}\right)=\frac{\partial}{\partial t}\left(\frac{1}{2}\overline{\tilde{V}_\alpha}^{L_y}\overline{\tilde{V}_\alpha}^{L_y}\overline{h}^{L_y}\right)+\left(\frac{1}{2}\overline{\tilde{V}_\alpha}^{L_y}\overline{\tilde{V}_\alpha}^{L_y}\right)\frac{\partial\overline{h}^{L_y}}{\partial t} \tag{A1}$$

$$\overline{\tilde{V}_\alpha}^{L_y}\frac{\partial}{\partial x}\left(\overline{\tilde{V}_\alpha}^{L_y}\overline{\tilde{V}_x}^{L_y}\overline{h}^{L_y}\right)=\frac{\partial}{\partial x}\left(\frac{1}{2}\overline{\tilde{V}_\alpha}^{L_y}\overline{\tilde{V}_\alpha}^{L_y}\overline{\tilde{V}_x}^{L_y}\overline{h}^{L_y}\right)+\frac{1}{2}\left(\overline{\tilde{V}_\alpha}^{L_y}\overline{\tilde{V}_\alpha}^{L_y}\right)\frac{\partial}{\partial x}\left(\overline{\tilde{V}_x}^{L_y}\overline{h}^{L_y}\right). \tag{A2}$$

[68] Using the continuity equation (30) for the longshore-averaged flow, we then get the local kinetic energy equation for the longshore-averaged flow as

$$\begin{aligned}&\frac{\partial}{\partial t}\left(\frac{1}{2}\overline{\tilde{V}_\alpha}^{L_y}\overline{\tilde{V}_\alpha}^{L_y}\overline{h}^{L_y}\right)+\frac{\partial}{\partial x}\left(\frac{1}{2}\overline{\tilde{V}_\alpha}^{L_y}\overline{\tilde{V}_\alpha}^{L_y}\overline{\tilde{V}_x}^{L_y}\overline{h}^{L_y}\right)\\&+\frac{\overline{\tilde{V}_\alpha}^{L_y}}{\rho}\frac{\partial\overline{S_{x\alpha}}^{L_y}}{\partial x}-\frac{\overline{\tilde{V}_\alpha}^{L_y}}{\rho}\frac{\partial\overline{T_{x\alpha}}^{L_y}}{\partial x}+\frac{\overline{\tilde{V}_\alpha}^{L_y}}{\rho}\frac{\partial\overline{L_{x\alpha}}^{L_y}}{\partial x}+\overline{\tilde{V}_\alpha}^{L_y}\frac{\overline{\tau_\alpha^B}^{L_y}}{\rho}\\&+g\overline{h}^{L_y}\overline{\tilde{V}_\alpha}^{L_y}\frac{\partial\overline{\overline{\zeta}}^{L_y}}{\partial x_\alpha}+\overline{\tilde{V}_\alpha}^{L_y}\frac{\partial}{\partial x}\overline{V'_\alpha V'_x}^{L_y}\overline{h}^{L_y}=0.\end{aligned} \tag{A3}$$

[69] When this equation is averaged in the longshore direction, we are left with several convective terms. However, these terms only move energy from one point to another. Therefore, in order to eliminate those terms, we integrate over L_x (the computation length in the cross-shore direction) as well, so that we get the energy equation for the entire computational domain.

[70] In the derivation, we also notice that

$$g\overline{h}^{L_y}\overline{\tilde{V}_\alpha}^{L_y}\frac{\partial\overline{\overline{\zeta}}^{L_y}}{\partial x_\alpha}=\frac{\partial}{\partial x_\alpha}\left(g\overline{h}^{L_y}\overline{\tilde{V}_\alpha}^{L_y}\overline{\overline{\zeta}}^{L_y}\right)+\frac{\partial}{\partial t}\frac{1}{2}g\overline{\overline{\zeta}}^{L_y\,2}, \tag{A4}$$

in which the continuity equation for the longshore-averaged flow motion equation (30) has been used.

[71] When integrating equation (A3) over L_x, the cross-shore extension of the computational domain, we find that all the divergence type terms go to zero when applying the boundary conditions.

[72] Furthermore, we write

$$\overline{\tilde{V}_\alpha}^{L_y}\frac{\partial}{\partial x}\overline{V'_\alpha V'_x}^{L_y}\overline{h}^{L_y}=\frac{\partial}{\partial x}\left(\overline{\tilde{V}_\alpha}^{L_y}\overline{V'_\alpha V'_x}^{L_y}\overline{h}^{L_y}\right)-\overline{V'_\alpha V'_x}^{L_y}\overline{h}^{L_y}\frac{\partial\overline{\tilde{V}_\alpha}^{L_y}}{\partial x}. \tag{A5}$$

We then get the kinematic energy equation for the longshore-averaged flow,

$$\begin{aligned}&\int_0^{L_x}\frac{\partial}{\partial t}\left(\frac{\overline{\tilde{V}_\alpha}^{L_y}\overline{\tilde{V}_\alpha}^{L_y}}{2}\overline{h}^{L_y}\right)dx+\int_0^{L_x}\frac{\partial}{\partial t}\frac{1}{2}g\overline{\overline{\zeta}}^{L_y\,2}dx\\&=\int_0^{L_x}\overline{V'_\alpha V'_x}^{L_y}\overline{h}^{L_y}\frac{\partial\overline{\tilde{V}_\alpha}^{L_y}}{\partial x}dx-\int_0^{L_x}\frac{\overline{\tilde{V}_\alpha}^{L_y}}{\rho}\frac{\partial\overline{S_{x\alpha}}^{L_y}}{\partial x}dx\\&+\int_0^{L_x}\frac{\overline{\tilde{V}_\alpha}^{L_y}}{\rho}\frac{\partial\overline{T_{x\alpha}}^{L_y}}{\partial x}dx-\int_0^{L_x}\frac{\overline{\tilde{V}_\alpha}^{L_y}}{\rho}\frac{\partial\overline{L_{x\alpha}}^{L_y}}{\partial x}dx\\&-\int_0^{L_x}\overline{\tilde{V}_\alpha}^{L_y}\frac{\overline{\tau_\alpha^B}^{L_y}}{\rho}dx,\end{aligned} \tag{A6}$$

where the wave-current interaction has been turned off.

[73] The local continuity and momentum equation, respectively, for the shear waves are obtained by subtracting equation (30) from equation (5), and equation (31) from equation (6),

$$\frac{\partial}{\partial x_\beta}\left(\tilde{V}'_\beta \overline{h}^{L_y}\right) = 0 \tag{A7}$$

$$\frac{\partial}{\partial t}\left(\tilde{V}'_\alpha \overline{h}^{L_y}\right) + \frac{\partial}{\partial x_\beta}\left(\tilde{V}'_\alpha \tilde{V}'_\beta \overline{h}^{L_y}\right) + \frac{1}{\rho}\frac{\partial S'_{\beta\alpha}}{\partial x_\beta} - \frac{1}{\rho}\frac{\partial T'_{\beta\alpha}}{\partial x_\beta} + \frac{1}{\rho}\frac{\partial L'_{\beta\alpha}}{\partial x_\beta} + \frac{\tau'^B_\alpha}{\rho}$$
$$+ \frac{\partial}{\partial x_\beta}\left(\tilde{V}'_\alpha \overline{\tilde{V}_\beta}^{L_y} \overline{h}^{L_y}\right) + \frac{\partial}{\partial x_\beta}\left(\overline{\tilde{V}_\alpha}^{L_y} \tilde{V}'_\beta \overline{h}^{L_y}\right) - \frac{\partial}{\partial x}\overline{\tilde{V}'_\alpha \tilde{V}'_x}^{L_y} \overline{h}^{L_y} = 0. \tag{A8}$$

[74] In the derivation above, we have assumed $h' = 0$ to simplify the derivation.

[75] Taking the dot product of the shear wave momentum equation (A8) and V'_α, we obtain the local kinetic energy equation for the shear waves. Performing longshore averaging and then integrating it over L_x, we get the kinetic energy equation for the shear waves equivalent to (A6).

$$\int_0^{L_x} \frac{\partial}{\partial t}\left(\frac{\overline{\tilde{V}'_\alpha \tilde{V}'_\alpha}^{L_y}}{2}\overline{h}^{L_y}\right)dx = \int_0^{L_x} \overline{\tilde{V}'_\alpha \tilde{V}'_x}^{L_y} \overline{h}^{L_y} \frac{\partial \overline{\tilde{V}_\alpha}^{L_y}}{\partial x}dx$$
$$+ \int_0^{L_x} \overline{\frac{\tilde{V}'_\alpha}{\rho}\frac{\partial T'_{\beta\alpha}}{\partial x_\beta}}^{L_y} dx - \int_0^{L_x} \overline{\frac{\tilde{V}'_\alpha}{\rho}\frac{\partial L'_{\beta\alpha}}{\partial x_\beta}}^{L_y} dx$$
$$- \int_0^{L_x} \overline{\tilde{V}'_\alpha \frac{\tau'^B_\alpha}{\rho}}^{L_y} dx. \tag{A9}$$

[76] In the above, we have used the continuity equations (30) and (A7), and identified

$$\overline{\tilde{V}'_\alpha \frac{\partial}{\partial t}\left(\tilde{V}'_\alpha \overline{h}^{L_y}\right)}^{L_y} = \frac{\partial}{\partial t}\left(\overline{\frac{1}{2}\tilde{V}'_\alpha V'_\alpha}^{L_y} \overline{h}^{L_y}\right) + \overline{\frac{1}{2}\tilde{V}'_\alpha V'_\alpha}^{L_y} \frac{\partial \overline{h}^{L_y}}{\partial t}, \tag{A10}$$

$$\overline{\tilde{V}'_\alpha \frac{\partial}{\partial x_\beta}\left(\tilde{V}'_\alpha \tilde{V}'_\beta \overline{h}^{L_y}\right)}^{L_y} = \frac{\partial}{\partial x_\beta}\left(\frac{1}{2}\overline{\tilde{V}'_\alpha V'_\alpha V'_\beta}^{L_y} \overline{h}^{L_y}\right) - \overline{\frac{1}{2}V'_\alpha V'_\alpha \frac{\partial V'_\beta \overline{h}^{L_y}}{\partial x_\beta}}^{L_y}$$
$$= \frac{\partial}{\partial x}\left(\frac{1}{2}\overline{\tilde{V}'_\alpha V'_\alpha V'_x}^{L_y} \overline{h}^{L_y}\right), \tag{A11}$$

$$\overline{\tilde{V}'_\alpha \frac{\partial}{\partial x_\beta}\tilde{V}'_\alpha \overline{\tilde{V}_\beta}^{L_y} \overline{h}^{L_y}}^{L_y} = \frac{\partial}{\partial x}\left(\frac{1}{2}\overline{V'_\alpha V'_\alpha}^{L_y} \overline{V_x}^{L_y} \overline{h}^{L_y}\right) + \frac{1}{2}\overline{\tilde{V}'_\alpha V'_\alpha}^{L_y} \frac{\partial \overline{\tilde{V}_x}^{L_y} \overline{h}^{L_y}}{\partial x}, \tag{A12}$$

$$\overline{\tilde{V}'_\alpha \frac{\partial}{\partial x_\beta}\tilde{V}'_\beta \overline{\tilde{V}_\alpha}^{L_y} \overline{h}^{L_y}}^{L_y} = \overline{\tilde{V}'_\alpha \tilde{V}'_\beta}^{L_y} \overline{h}^{L_y} \frac{\partial \overline{\tilde{V}_x}^{L_y}}{\partial x} + \overline{\tilde{V}'_\alpha \overline{\tilde{V}_\alpha}^{L_y} \frac{\partial V'_\beta \overline{h}^{L_y}}{\partial x_\beta}}^{L_y}$$
$$= \overline{\tilde{V}'_\alpha \tilde{V}'_\beta}^{L_y} \overline{h}^{L_y} \frac{\partial \overline{\tilde{V}_x}^{L_y}}{\partial x}. \tag{A13}$$

[77] The divergence theorem and the boundary conditions have been used to eliminate the convective terms.

Appendix B: Derivation of the Shear Wave Enstrophy Equation

[78] According to equation (24),

$$\tilde{\omega}(x, y, t) = \overline{\tilde{\omega}(x, y, t)}^{L_y} + \tilde{\omega}'(x, y, t), \tag{B1}$$

and $\overline{\tilde{\omega}(x, y, t)}^{L_y}$ is the longshore-averaged vorticity.

$$\overline{\tilde{\omega}(x, y, t)}^{L_y} = \frac{1}{L_y}\int_0^{L_y} \tilde{\omega}(x, y, t)dy. \tag{B2}$$

[79] Substituting equations (B1) and (B2) into equation (37) and performing longshore averaging, we then obtained the longshore-averaged vorticity transport equation,

$$\frac{\partial \overline{\tilde{\omega}_z}^{L_y}}{\partial t} + \overline{\tilde{V}_x}^{L_y} \frac{\partial \overline{\tilde{\omega}_z}^{L_y}}{\partial x} + \overline{\tilde{\omega}_z}^{L_y} \frac{\partial \overline{\tilde{V}_\beta}^{L_y}}{\partial x_\beta}$$
$$= -\varepsilon_{x\alpha z}\frac{\partial}{\partial x}\frac{1}{\rho \overline{h}^{L_y}}\frac{\partial}{\partial x}\left(\overline{S_{x\alpha}}^{L_y} - \overline{T_{x\alpha}}^{L_y} + \overline{L_{x\alpha}}^{L_y}\right)$$
$$-\varepsilon_{x\alpha z}\frac{\partial}{\partial x}\frac{\overline{\tau^B_\alpha}^{L_y}}{\rho \overline{h}^{L_y}} - \overline{\tilde{V}'_\beta \frac{\partial \tilde{\omega}'_z}{\partial x_\beta}}^{L_y} - \overline{\tilde{\omega}'_z \frac{\partial \tilde{V}'_\beta}{\partial x_\beta}}^{L_y}. \tag{B3}$$

[80] The vorticity transport equation for the shear waves is obtained by subtracting equation (B4) from equation (37),

$$\frac{\partial \tilde{\omega}'_z}{\partial t} + \tilde{V}'_\beta \frac{\partial \tilde{\omega}'_z}{\partial x_\beta} + \tilde{V}'_x \frac{\partial \overline{\tilde{\omega}_z}^{L_y}}{\partial x} + \overline{\tilde{V}_\beta}^{L_y} \frac{\partial \tilde{\omega}'_z}{\partial x_\beta} + \tilde{\omega}'_z \frac{\partial \tilde{V}'_\beta}{\partial x_\beta}$$
$$+ \overline{\tilde{\omega}_z}^{L_y} \frac{\partial \tilde{V}'_\beta}{\partial x_\beta} + \tilde{\omega}'_z \frac{\partial \overline{\tilde{V}_x}^{L_y}}{\partial x}$$
$$= -\varepsilon_{\beta\alpha z}\frac{\partial}{\partial x_\beta}\frac{1}{\rho \overline{h}^{L_y}}\frac{\partial}{\partial x_\gamma}\left(-T'_{\gamma\alpha} + L'_{\gamma\alpha}\right) - \varepsilon_{x\alpha z}\frac{\partial}{\partial x}\frac{\tau'^B_\alpha}{\rho \overline{h}^{L_y}}$$
$$+ \overline{\tilde{V}'_\beta \frac{\partial \tilde{\omega}'_z}{\partial x_\beta}}^{L_y} + \overline{\tilde{\omega}'_z \frac{\partial \tilde{V}'_\beta}{\partial x_\beta}}^{L_y}. \tag{B4}$$

[81] Similar to the shear wave kinetic energy equation, the depth-integrated enstrophy equation for the shear waves is obtained by taking a dot product of equation (B4) and $\tilde{\omega}'_z \overline{h}^{L_y}$, then performing the longshore averaging. The continuity equations for the longshore-averaged flow and the shear waves, and

$$\overline{\tilde{\omega}'_z \overline{h}^{L_y} \frac{\partial \tilde{\omega}'_z}{\partial t}}^{L_y} = \overline{h}^{L_y} \frac{\partial}{\partial t}\left(\frac{1}{2}\overline{\tilde{\omega}'_z \tilde{\omega}'_z}^{L_y}\right)$$
$$= \frac{\partial}{\partial t}\left(\frac{1}{2}\overline{\tilde{\omega}'_z \tilde{\omega}'_z}^{L_y} \overline{h}^{L_y}\right) - \frac{1}{2}\overline{\tilde{\omega}'_z \tilde{\omega}'_z}^{L_y} \frac{\partial \overline{h}^{L_y}}{\partial t}, \tag{B5}$$

$$\overline{\tilde{\omega}'_z \overline{h}^{L_y} \tilde{V}'_\beta \frac{\partial \tilde{\omega}'_z}{\partial x_\beta}}^{L_y} = \overline{\tilde{V}'_\beta \overline{h}^{L_y} \frac{\partial}{\partial x_\beta}\frac{1}{2}\tilde{\omega}'_z \tilde{\omega}'_z}^{L_y}$$
$$= \frac{\partial}{\partial x}\left(\frac{1}{2}\overline{\tilde{\omega}'_z \tilde{\omega}'_z V'_x}^{L_y} \overline{h}^{L_y}\right) - \overline{\frac{1}{2}\tilde{\omega}'_z \tilde{\omega}'_z \frac{\partial}{\partial x_\beta}\left(\tilde{V}'_\beta \overline{h}^{L_y}\right)}^{L_y}$$
$$= \frac{\partial}{\partial x}\left(\frac{1}{2}\overline{\tilde{\omega}'_z \tilde{\omega}'_z V'_x}^{L_y} \overline{h}^{L_y}\right), \tag{B6}$$

$$\begin{aligned}\overline{\tilde{\omega}'_z \overline{h}^{L_y} \overline{\tilde{V}_\beta}^{L_y} \frac{\partial \tilde{\omega}'_z}{\partial x_\beta}}^{L_y} &= \overline{\tilde{V}_x}^{L_y} \overline{h}^{L_y} \frac{\partial}{\partial x} \frac{1}{2} \overline{\tilde{\omega}'_z \tilde{\omega}'_z}^{L_y} \\ &= \frac{\partial}{\partial x}\left(\frac{1}{2} \overline{\tilde{\omega}'_z \tilde{\omega}'_z}^{L_y} \overline{\tilde{V}_x}^{L_y} \overline{h}^{L_y}\right) - \frac{1}{2} \overline{\tilde{\omega}'_z \tilde{\omega}'_z}^{L_y} \frac{\partial}{\partial x}\left(\overline{V_x}^{L_y} \overline{h}^{L_y}\right),\end{aligned} \tag{B7}$$

$$\overline{\tilde{\omega}'_z \overline{h}^{L_y} \overline{\tilde{V}'_\beta \frac{\partial \tilde{\omega}'_z}{\partial x_\beta}}^{L_y}}^{L_y} = 0, \tag{B8}$$

$$\overline{\tilde{\omega}'_z \overline{h}^{L_y} \overline{\omega'_z \frac{\partial \tilde{V}'_\beta}{\partial x_\beta}}^{L_y}}^{L_y} = 0, \tag{B9}$$

are used in the derivation. Integrating the enstrophy equation in the cross-shore direction, and using the boundary condition, we get the enstrophy equation for the shear waves in the entire domain.

$$\begin{aligned}\int_0^{L_x} \frac{\partial}{\partial t} \frac{\overline{\tilde{\omega}'_z \tilde{\omega}'_z}^{L_y} \overline{h}^{L_y}}{2} dx = &- \int_0^{L_x} \overline{\tilde{\omega}'_z \tilde{V}'_x}^{L_y} \overline{h}^{L_y} \frac{\partial \overline{\tilde{\omega}_z}^{L_y}}{\partial x} dx \\ &+ \int_0^{L_x} \varepsilon_{\beta\alpha z} \overline{h}^{L_y} \overline{\tilde{\omega}'_z \frac{\partial}{\partial x_\beta} \frac{1}{\rho \overline{h}^{L_y}} \frac{\partial T'_{\gamma\alpha}}{\partial x_\gamma}}^{L_y} dx \\ &- \int_0^{L_x} \varepsilon_{\beta\alpha z} \overline{h}^{L_y} \overline{\tilde{\omega}'_z \frac{\partial}{\partial x_\beta} \frac{1}{\rho \overline{h}^{L_y}} \frac{\partial L'_{\gamma\alpha}}{\partial x_\gamma}}^{L_y} dx \\ &- \int_0^{L_x} \varepsilon_{\beta\alpha z} \overline{h}^{L_y} \overline{\tilde{\omega}'_z \frac{\partial}{\partial x_\beta} \frac{\tau'^B_\alpha}{\rho \overline{h}^{L_y}}}^{L_y} dx \\ &- \int_0^{L_x} \overline{h}^{L_y} \overline{\tilde{\omega}'_z \left(\tilde{\omega}'_z \frac{\partial \tilde{V}'_\beta}{\partial x_\beta} + \overline{\tilde{\omega}_z}^{L_y} \frac{\partial \tilde{V}'_\beta}{\partial x_\beta} + \tilde{\omega}'_z \frac{\partial \overline{\tilde{V}_x}^{L_y}}{\partial x}\right)}^{L_y} dx.\end{aligned} \tag{B10}$$

[82] **Acknowledgments.** Thanks are due to Nick Dodd and Özkan-Haller for providing the topography data files. This research has been sponsored by Office of Naval Research (ONR), Coastal Dynamics Program under grant N00014-99-1-0291, and National Oceanographic Partnership Program (NOPP) by ONR (contract N0014-99-1-1051). The U.S. government is authorized to produce and distribute reprints for government purposes not withstanding any copyright notation that may appear herein.

References

Allen, J. S., P. A. Newberger, and R. A. Holman, Nonlinear shear instabilities of alongshore currents on plane beaches, *J. Fluid Mech.*, *310*, 181–213, 1996.

Battjes, J. A., Modeling of turbulence in the surf zone, paper presented at Symposium on Modeling Techniques, Am. Soc. Civ. Eng., Reston, Va., 1975.

Bowen, A. J., and R. A. Holman, Shear instabilities of the mean longshore current: 1. Theory, *J. Geophys. Res.*, *94*(C12), 18,023–18,030, 1989.

Coffey, F. C., and P. Nielsen, Aspects of wave current boundary layer flows, paper presented at 19th International Conference on Coastal Engineering, Am. Soc. Civ. Eng., Reston, Va., 1984.

Deigaard, R., E. D. Christensen, J. S. Damgaard, and J. Fredsoe, Numerical simulation of finite amplitude shear waves and sediment transport, paper presented at 24th International Conference on Coastal Engineering, Am. Soc. Civ. Eng., Reston, Va., 1994.

Dodd, N., On the destabilization of a longshore current on a plane beach: Bottom shear stress, critical conditions and onset of instability, *J. Geophys. Res.*, *99*(C1), 811–824, 1994.

Dodd, N., and E. B. Thornton, Growth and energetics of shear waves in the nearshore, *J. Geophys. Res.*, *95*(C9), 16,075–16,083, 1990.

Dodd, N., J. Oltman-Shay, and E. B. Thornton, Shear instabilities In the long-shore-current: A comparison of observation and theory, *J. Phys. Oceanogr.*, *22*(1), 62–82, 1992.

Dodd, N., V. Iranzo, and A. Reniers, Shear instabilities of wave-driven alongshore currents, *Rev. Geophys.*, *38*(4), 437–463, 2000.

Falqués, A., and V. Iranzo, Numerical simulation of vorticity waves in the nearshore, *J. Geophys. Res.*, *99*(C1), 825–841, 1994.

Falqués, A., V. Iranzo, and M. Caballeria, Shear instability of longshore currents: Effects of dissipation and non-linearity, paper presented at 24th International Conference on Coastal Engineering, Am. Soc. Civ. Eng., Reston, Va., 1994.

Kirby, J., and R. Dalrymple, Combined refraction/diffraction model REF/DIF 1, version 2.5, *Internal Rep. CACR-94-22*, Cent. for Appl. Coastal Res., Univ. of Del., Newark, Del., 1994.

Nadaoka, K., and T. Kondoh, Laboratory measurements of velocity field structure in surf zone by LDV, *Coastal Eng. Jpn.*, *25*, 125–145, 1982.

Oltman-Shay, J., P. A. Howd, and W. A. Birkemeier, Shear instabilities of the mean longshore current: 2. Field observations, *J. Geophys. Res.*, *94*(C12), 18,031–18,042, 1989.

Özkan-Haller, T., and J. T. Kirby, Nonlinear evolution of shear instabilities of the longshore current: A comparison of observations and computations, *J. Geophys. Res.*, *104*(C11), 25,953–25,984, 1999.

Putrevu, U., and I. A. Svendsen, Shear instability of longshore currents: A numerical study, *J. Geophys. Res.*, *97*(C5), 7283–7303, 1992.

Putrevu, U., and I. A. Svendsen, Three-dimensional dispersion of momentum in wave-induced nearshore currents, *Eur. J. Mech.*, 409–427, 1999.

Sancho, F., and I. A. Svendsen, Shear waves over longshore nonuniform barred beached, paper presented at 26th International Conference on Coastal Engineering, Am. Soc. Civ. Eng., Reston, Va., 1998.

Slinn, D. N., J. A. Allen, P. A. Newberger, and R. A. Holman, Nonlinear shear instabilities of alongshore currents over barred beaches, *J. Geophys. Res.*, *103*(C9), 18,357–18,379, 1998.

Svendsen, I. A., Mass flux and undertow in a surf zone, *Coastal Eng.*, *8*, 347–365, 1984.

Svendsen, I. A., and U. Putrevu, Nearshore mixing and dispersion, *Proc. R. Soc. London, Ser. A*, *445*, 561–576, 1994.

Svendsen, I. A., H. A. Schäffer, and J. Buhr Hansen, The interaction between undertow and the boundary layer flow on a beach, *J. Geophys. Res.*, *92*(C11), 11,845–11,856, 1987.

Svendsen, I. A., K. Haas, and Q. Zhao, Quasi-3D nearshore circulation model SHORECIRC, *Internal Rep. CACR-02-01*, Cent. for Appl. Coastal Res., Univ. of Del., Newark, Del., 2002.

Taylor, G. I., The dispersion of matter in a turbulent flow through a pipe, *Proc. R. Soc. London, Ser. A*, *223*, 446–468, 1954.

Van Dongeren, A., and I. A. Svendsen, Nonlinear and 3D effects in leaky infragravity waves, *Coastal Eng.*, *41*, 467–496, 2000.

K. Haas, Regional Engineering Program, Georgia Institute of Technology, 6001 Chatham Center Drive, Suite 350, Savannah, GA 31405, USA.

I. A. Svendsen and Q. Zhao, Ocean Engineering Laboratory, Center for Applied Coastal Research, University of Delaware, Newark, DE 19716, USA. (zhao@coastal.udel.edu)